

REVIEW

An introductory review of the thermal structure of subduction zones: II. Numerical approach and validation

Cian R. Wilson* and Peter E. van Keken

*Correspondence:

cwilson@carnegiescience.edu
 Earth and Planets Laboratory,
 Carnegie Institution for Science,
 5241 Broad Branch Road, NW,
 Washington DC 20015, USA.
 Full list of author information is
 available at the end of the article

Abstract

The thermal structure of subduction zones is fundamental to our understanding of the physical and chemical processes that occur at active convergent plate margins. These include magma generation and related arc volcanism, shallow and deep seismicity, and metamorphic reactions that can release fluids.

Computational models can predict the thermal structure to great numerical precision when models are fully described but this does not guarantee accuracy or applicability. In a trio of companion papers the construction of thermal subduction zone models, their use in subduction zone studies, and their link to geophysical and geochemical observations is explored. In this part II the finite element techniques that can be used to predict thermal structure are discussed in an introductory fashion along with their verification and validation.

Keywords

Geodynamics, Plate tectonics, Finite element methods, Subduction zone metamorphism, Arc volcanism

1
2

3 1 Introduction to Part II

4 This paper is a companion to van Keken and Wilson “An introductory review of
 5 the thermal structure of subduction zones: I–motivation and selected examples”
 6 (van Keken and Wilson, 2023, hereafter called Part I) and van Keken and Wilson
 7 “An introductory review of the thermal structure of subduction zones: III. Com-
 8 parison between models and observations” (hereafter referred to as part III). A
 9 preprint to part III is available in the Supplementary Information

10 Combined these articles provide an introduction to the use of thermal models
 11 and observational constraints to aid our understanding of the dynamics, structure,
 12 and evolution of subduction zones from a geophysical, geochemical, and petrological
 13 perspective. In Part I we provided the motivation for these studies, fundamental con-
 14 straints on subduction zone geometry and thermal structure, and a limited overview
 15 of existing thermal models. In this article we will provide a discussion of the use
 16 of the finite element method to discretize partial differential equations needed for
 17 subduction zone modeling, present open-source software, and discuss validation &
 18 verification approaches to understand the reliability of the thermal models.

19 Our approach will be similar to that in Part I – we strive to make this intro-
 20 duction accessible to advanced undergraduates, graduate students, and professionals
 21 from outside geodynamics. This will, hopefully, make the reader able to establish
 22 a fundamental understanding of what is required for numerical modeling of the
 23 thermal structure of subduction zones.

24 While we focus on the use of finite element methods to solve the governing equa-
 25 tions we acknowledge that significant and important studies have been published
 26 that use finite difference (FD) or finite volume (FV) methods. An introduction to
 27 the use of FD methods in geodynamical applications is provided by Gerya (2019).
 28 A broader overview of computational methods for geodynamics including FV is in
 29 Ismail-Zadeh and Tackley (2010). A useful overview of the use of finite element
 30 methods specifically for mantle convection modeling with a comparison to FD and
 31 FV methods is in Zhong et al. (2015). As we will see, finite element methods can be
 32 used to discretize complex geometries, which provides a significant advantage for
 33 subduction zone modeling over FD and FV methods.

34 In section 2 we first describe how finite element approaches to solve common
 35 linear partial differential equations such as the Poisson and Stokes equations are con-
 36 structed. We then apply this to dynamical models that rely on solving the Stokes
 37 and heat equations, which include a standard convection benchmark and a new
 38 simplified subduction zone benchmark. The latter will be used to quantify the pre-
 39 cision with which we can predict the subduction zone thermal structure using a
 40 kinematic-dynamic approach.

41 2 Finite element modeling

42 2.1 General formulation of the finite element solution of partial differential equations

43 The goal of the numerical models discussed here is to find the approximate solutions
 44 of partial differential equations (PDEs) in a spatial domain denoted by Ω , with
 45 boundaries $\partial\Omega$, representing some part of the Earth, say, a cross-section through
 46 a subduction zone. These PDEs can be time-dependent, nonlinear, or nonlinearly
 47 coupled to other PDEs. To sketch out how we can discretize the PDEs with finite
 48 elements we will first assume that we have linear PDEs of the general form

$$49 \quad L(u) = f \quad \text{in } \Omega \quad (1)$$

50 where L is a linear differential operator, f some right-hand side function, and $u =$
 51 $u(\vec{x}, t)$ the solution we seek to approximate over space \vec{x} and time t . In addition to
 52 (1) we require boundary conditions of the form

$$53 \quad J(u) = g \quad \text{on } \partial\Omega \quad (2)$$

54 where J is a linear differential operator and g is a function describing how u and/or
 55 its derivatives behave on the boundary. Efficient computer solution of the linear
 56 differential problem (1)–(2) relies on discretizing the domain Ω into a set of de-
 57 grees of freedom (DOFs) or values at “nodal” points in the domain at which the
 58 approximate solution is sought. This discretization facilitates the translation of the
 59 governing equations from differential to algebraic matrix-vector form. Discretization
 60 schemes differ in how they organize and distribute the degrees of freedom onto a
 61 mesh or grid of points across the domain.

62 Finite difference methods distribute DOFs at points in Ω and construct ap-
 63 proximate derivatives by taking the differences between the values of neighboring

64 points (along connecting lines in a mesh of points). This is made easier if the DOFs
 65 are organized in a regular or structured grid. Finite volume methods construct control
 66 volumes surrounding the degrees of freedom and, rather than approximating the
 67 derivatives, they consider the fluxes through the control volume boundaries between
 68 neighboring degrees of freedom. This means that the DOFs can be distributed in
 69 an unstructured way, but achieving higher orders of accuracy with FV methods is
 70 easier on structured meshes. The finite element method (FEM), on the other hand,
 71 tessellates the domain with polygonal elements and then distributes DOFs relative
 72 to these elements. The order of accuracy is then controlled by the number and the
 73 distribution of DOFs within an element, which can themselves be arranged in an
 74 unstructured pattern.

75 Formally, the FEM approximates u by \tilde{u} , the solution's representation in a
 76 function space on the mesh where

$$77 \quad \tilde{u}(\vec{x}, t) = \sum_j \phi_j(\vec{x}) u_j(t) \quad (3)$$

78 Here, u_j are coefficients that as indicated can be time-dependent but do not depend
 79 on space. The shape functions ϕ_j are a function of space but generally independent
 80 of time. The index j indicates the number of the shape function on the mesh and
 81 is associated with the number of the nodal point or element number it is associ-
 82 ated with. In this manuscript, we will principally discuss so-called Lagrange shape
 83 functions which define ϕ_j as a polynomial over an element with a value of 1 at a
 84 single nodal point and a value of 0 at all other points associated with the degrees of
 85 freedom such that $\sum_j \phi_j = 1$ (see Figure 1). The shape functions can be of arbitrary
 86 order and can have various conditions on their continuity across or in between el-
 87 ements. We will focus principally on linear Lagrange shape functions (denoted by
 88 P1) and quadratic Lagrange shape functions (denoted by P2) that are continuous
 89 between mesh elements. Our choice of Lagrange shape functions means that u_j are
 90 the actual values of the solution in (3). With other forms of the shape function
 91 u_j are instead interpolation weights that are used to construct the solution values.
 92 The split of temporal and spatial dependence above is typical in geodynamic ap-
 93 plications but not required. Given the “trial” solution function (3), finite element
 94 methods pose (1) as a residual $R(\tilde{u})$:

$$95 \quad R(\tilde{u}) = L(\tilde{u}) - f \quad (4)$$

96 The residual is minimized in a weighted average sense by multiplying the residual
 97 with weighting test function, \tilde{u}_t , integrating over the domain of interest, and setting
 98 this to zero:

$$99 \quad \int \tilde{u}_t R(\tilde{u}) d\Omega = 0 \quad (5)$$

100 The test functions \tilde{u}_t can be independent of the functions ϕ_j that span the func-
 101 tion space of the trial function, but in the widely used Galerkin approach the test
 102 functions are restricted to be in the same function space such that

$$103 \quad \tilde{u}_t(\vec{x}, t) = \sum_i \phi_i(\vec{x}) u_{ti}(t) \quad (6)$$

104 Since the method is valid for all \tilde{u}_t we can dispense with the test function values at
 105 the DOFs, u_{ti} , and the minimization function can be written as

$$106 \quad \int \phi_i R(\tilde{u}) d\Omega = 0 \quad \text{for all } i \quad (7)$$

107 Given a domain with n DOFs such that $i, j=1, \dots, n$, combining (7) with (3) and
 108 results in a matrix-vector system of the form

$$109 \quad \mathbf{S}\mathbf{u} = \mathbf{f} \quad (8)$$

110 where \mathbf{S} is a $n \times n$ matrix, \mathbf{f} is the right-hand side vector of length n and \mathbf{u} is the
 111 solution vector of values or weights at the DOFs

$$112 \quad \mathbf{S} = S_{ij} = \int \phi_i L(\phi_j) d\Omega \quad (9)$$

$$113 \quad \mathbf{f} = f_i = \int f \phi_i d\Omega \quad (10)$$

$$114 \quad \mathbf{u} = u_j \quad (11)$$

116 where we can move the solution values out of the integral in (7) due to the linear
 117 nature of L . For elliptic problems, \mathbf{S} is sometimes called the stiffness matrix and \mathbf{f}
 118 the load vector because the finite element method was initially used in structural
 119 problems where \mathbf{u} typically represents a displacement. It expresses how for a given
 120 load \mathbf{f} the stiffness of the structure, as expressed by the coefficients in the stiffness
 121 matrix \mathbf{S} , limits the displacement \mathbf{u} of nodes in a structure. Note that in the above
 122 summary we have glossed over the imposition of boundary conditions (2), which
 123 must be incorporated into the residual (4), trial (3) and test (6) functions. Assuming
 124 that the boundary conditions are correctly implemented, that the problem (1)–(2)
 125 is well-posed, and that the discretization is adequate, then the discrete approximate
 126 solution \mathbf{u} (11) can be found through direct or iterative solution of (8).

127 The ease with which finite elements can be used on an unstructured mesh
 128 gives them one of their primary advantages for subduction zone modeling - being
 129 able to tessellate complex geometries. This is of particular importance when, for
 130 example, explicitly discretizing the subducting slab surface, surface topography, or
 131 crustal interfaces in the overriding plate. In addition, grid refinement can be used
 132 where strong gradients in solutions exist (such as at the top of the slab when it
 133 gets in contact with the hot mantle wedge; see Figure 1b in part I) and coarse
 134 grids can be used where the solutions are relatively constant, leading to improved
 135 overall computational efficiency compared to methods that require a structured
 136 discretization of space. Another advantage of the finite element method, that we
 137 will see below, is the natural way in which boundary conditions can be implemented.

138 For Lagrange bases increasing the order of the polynomial of ϕ_j increases the
 139 number of DOFs per element (see Figure 1) and increases the order of accuracy
 140 of the solution. The shape functions may be continuous or discontinuous between
 141 elements but each ϕ_j ideally has compact support, meaning that the basis function

142 associated with a degree of freedom only has nonzero values in the elements imme-
 143 diately surrounding the DOF. It is this property that ensures the matrix \mathbf{S} (9) is
 144 sparse in the final discrete system of equations (8).

145 We provide practical examples that show how to construct (8) using finite
 146 elements. Our goal is to demonstrate the flexibility and power of the FEM with-
 147 out giving an exhaustive introduction or rigorous mathematical derivation of the
 148 method. Practical introductions to the FEM can be found in Johnson (1987) and
 149 Logan (2017). More mathematically founded descriptions of the FEM can be found
 150 in Oden and Reddy (1976), Hughes (1987), and Strang and Fix (2008). Some of
 151 these texts are available in affordable Dover reprints.

152 2.2 Construction of finite element models

153 2.2.1 Examples of partial differential equations solved by the FEM

154 The exact set of equations that needs to be solved to make predictions of the ther-
 155 mal structure of subduction zones using a kinematic-dynamic approach is provided
 156 in section 2.3.1. These are derived from the fundamental equations governing the
 157 conservation of mass, momentum, and thermal energy. The conservation of mass
 158 and momentum lead, under a number of simplifying assumptions (that we will not
 159 discuss in detail but that can be found in fundamental textbooks such as Turcotte
 160 and Schubert, 2002) to the nondimensional Stokes equation and the condition of
 161 incompressibility

$$162 \quad -\nabla \cdot \left(2\eta \frac{\nabla \vec{v} + \nabla \vec{v}^T}{2} \right) + \nabla P = \vec{f}_B \quad (12)$$

$$163 \quad \nabla \cdot \vec{v} = 0 \quad (13)$$

165 Given a viscosity, η , and a buoyancy force, \vec{f}_B , that can depend on temperature
 166 and composition, the Stokes equation balances viscous, pressure, and buoyancy
 167 forces. Further imposition of the incompressibility constraint (13) allows us to find
 168 the velocity, \vec{v} , and pressure, P . The conservation of thermal energy leads to the
 169 nondimensional heat advection-diffusion equation

$$170 \quad \rho c_p \left(\frac{\partial T}{\partial t} + \vec{v} \cdot \nabla T \right) = \nabla \cdot (k \nabla T) + H \quad (14)$$

171 which, given the density, ρ , heat capacity, c_p , and thermal conductivity, k , bal-
 172 ances the transport of heat by diffusion and advection with heat production, H .
 173 The heat equation can be modeled to be stationary (by assuming $\frac{\partial T}{\partial t} = 0$) and the
 174 Stokes equation can be nonlinear due to the dependence of the viscosity on stress.
 175 The Stokes equation with the incompressibility constraint are generally nonlinearly
 176 coupled with the heat advection-diffusion equation.

177 In this section, rather than immediately solving the full nonlinear set of equa-
 178 tions, we will provide examples of how to solve (12)–(14) one by one, under various
 179 simplifying assumptions, before embarking on a fully coupled problem. We will start
 180 with a simple worked-out example of a 1D Poisson equation which is arguably the
 181 simplest form of (14) under the assumption of zero velocity, which also eliminates

182 (12)–(13) entirely. This will include the generation of shape functions, construction
 183 of the matrix-vector system, solution on a coarse mesh, comparisons between linear
 184 and quadratic elements, and convergence tests. This section is particularly intended
 185 for those new to finite element methodology and nomenclature. Those comfortable
 186 with basic FEM concepts but interested in the weak form formulation of PDEs and
 187 their FEM solution can skip forward to section 2.2.3 where we describe the FEM
 188 implementation and software availability. This is followed by the extension of the
 189 Poisson heat-diffusion problem to more than one dimension and the solution of the
 190 linear Stokes equation for a traditional cornerflow problem, neglecting temperature
 191 effects. We then combine the heat and Stokes equation in coupled problems using a
 192 standard mantle convection benchmark before focusing on simplified models of sub-
 193 duction zones. Unless explicitly mentioned otherwise we will assume in all examples
 194 below that the equations are in nondimensional form.

195 Section 2.3 derives (12)–(14) from their dimensional form and discusses how
 196 they are used in kinematic-dynamic subduction zone models. Readers who are more
 197 interested in understanding how different modeling approaches for subduction zone
 198 thermal structure compare or how the models compare to observations are invited
 199 to skip forward to part III.

200 2.2.2 1D Poisson

201 As an introductory and simplified example we will solve the Poisson equation on
 202 a 1D domain of unit length, $\Omega = [0, 1]$. This can be derived from the steady-state
 203 form of (14) by assuming zero velocity and a constant thermal conductivity, and
 204 seeking the approximate solution of

$$205 \quad -\frac{d^2T}{dx^2} = f \quad (15)$$

207 where we choose for this example $f = \frac{H}{k} = \frac{1}{4}\pi^2 \sin\left(\frac{\pi x}{2}\right)$. At the boundaries, $x=0$ and
 208 $x=1$, we apply as boundary conditions (2)

$$209 \quad T = 0 \quad \text{at } x = 0 \quad (16)$$

$$210 \quad \frac{dT}{dx} = 0 \quad \text{at } x = 1 \quad (17)$$

212 The first boundary condition is an example of an essential or Dirichlet boundary
 213 condition where we specify the value of the solution. The second boundary condition
 214 is an example of a natural or Neumann boundary condition that can be interpreted
 215 to mean that the solution is symmetrical around $x=1$. We will return to the vari-
 216 ous types of boundary conditions and their implementation in a later section. The
 217 analytical solution to (15) with given boundary conditions (16)–(17) is simply

$$218 \quad T = \sin\left(\frac{\pi x}{2}\right) \quad (18)$$

219 Minimization of the residual $R(\tilde{T})$ following (4) and (7) leads to

$$220 \quad -\int_0^1 \phi_i \frac{d^2\tilde{T}}{dx^2} dx = \int_0^1 \phi_i f dx \quad i = 1, \dots, n \quad (19)$$

221 By integrating the first term by parts we find

$$222 \quad \int_0^1 \frac{d\phi_i}{dx} \frac{d\tilde{T}}{dx} dx - \left[\phi_i \frac{d\tilde{T}}{dx} \right]_0^1 = \int_0^1 \phi_i f dx \quad i = 1, \dots, n \quad (20)$$

223 where the second term can be dropped because at $x=1$ we require $\frac{d\tilde{T}}{dx}=0$ and the
224 solution at $x=0$ is known, $\tilde{T}=0$, so can be lifted from the resulting matrix equation.

225 We can find the solution at the DOFs, T_j , from the discrete $n \times n$ matrix-vector
226 system (8) where now

$$227 \quad \mathbf{S} = S_{ij} = \int_0^1 \frac{d\phi_i}{dx} \frac{d\phi_j}{dx} dx \quad (21)$$

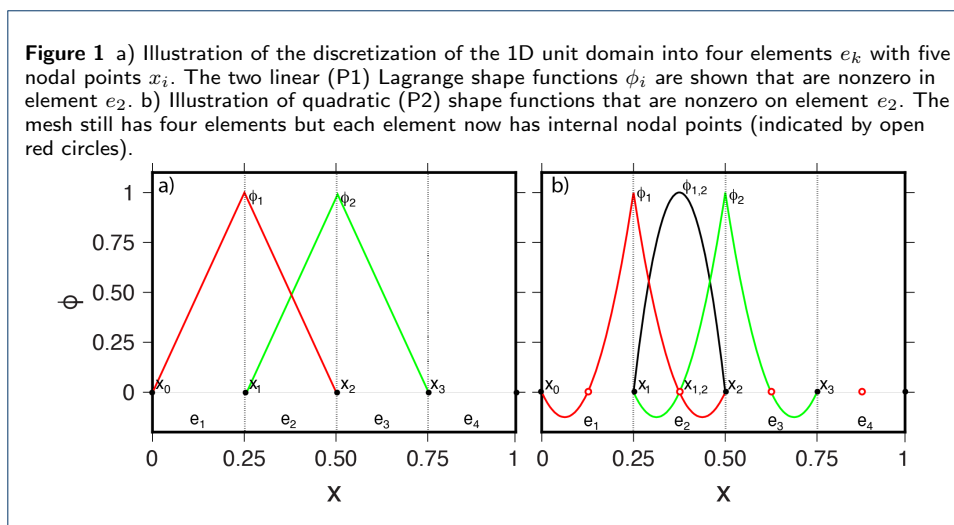
$$228 \quad \mathbf{f} = f_i = \int_0^1 \phi_i f dx \quad (22)$$

$$229 \quad \mathbf{u} = \mathbf{T} = T_j \quad (23)$$

231 where \mathbf{T} has components T_j that define the continuous approximate solution

$$232 \quad \tilde{T}(x) = \sum_{j=1}^n \phi_j(x) T_j \quad (24)$$

and $T_0=0$.



233

234 The domain is divided into n_e elements of equal length, $\Delta x = \frac{1}{n_e}$, with elements
235 e_i and degrees of freedom T_i ordered from $x=0$ to $x=1$. This introduces nodal points
236 x_i , $0 \leq i \leq n$ (see Figure 1a). A simple assumption for the Lagrange shape functions
237 ϕ_i is that the shape functions are linear within the elements. Such functions within
238 a given element e_i ($x_{i-1} \leq x \leq x_i$), $1 \leq i \leq n_e$, are

$$239 \quad \lambda_{i-1} = \frac{x_i - x}{\Delta x}, \quad \lambda_i = \frac{x - x_{i-1}}{\Delta x} \quad (25)$$

240 The functions λ_j are zero for all elements except e_j and e_{j+1} ($\forall e_i \notin \{e_j, e_{j+1}\}$). Since
 241 they fit the definition of linear Lagrange functions and we can write $\phi_i = \lambda_i$. Within
 242 a given element e_i we can construct the interpolated approximate solution for \tilde{T}
 243 from \mathbf{T} using

$$244 \quad \tilde{T}(x) = T_{i-1}\phi_{i-1}(x) + T_i\phi_i(x) \quad (26)$$

245 The expression is compact because all shape functions other than ϕ_{i-1} and ϕ_i are
 246 zero within this element. Note that the derivatives of the shape functions in this
 247 element are simply

$$248 \quad \frac{d\phi_{i-1}}{dx} = -\frac{1}{\Delta x} \quad , \quad \frac{d\phi_i}{dx} = \frac{1}{\Delta x} \quad (27)$$

249 which allows for easy evaluation of the matrix coefficients.

250 Evaluation of the integrals in (21) and (22) allows us to construct (8) as

$$251 \quad \frac{1}{\Delta x^2} \begin{pmatrix} 2 & -1 & 0 & \cdots & 0 & 0 & 0 \\ -1 & 2 & -1 & \cdots & 0 & 0 & 0 \\ \vdots & \vdots & \vdots & & \vdots & \vdots & \vdots \\ 0 & 0 & 0 & \cdots & -1 & 2 & -1 \\ 0 & 0 & 0 & \cdots & 0 & -1 & 1 \end{pmatrix} \begin{pmatrix} T_1 \\ T_2 \\ \vdots \\ T_{n-1} \\ T_n \end{pmatrix} = \begin{pmatrix} \int f\phi_1 dx \\ \int f\phi_2 dx \\ \vdots \\ \int f\phi_{n-1} dx \\ \int f\phi_n dx \end{pmatrix} \quad (28)$$

252 The integral in the right-hand side vector \mathbf{f} can be found analytically or through
 253 numerical integration. The matrix may look familiar to those acquainted with finite
 254 difference approximations to the 1D Poisson equation where d^2T/dx^2 is approxi-
 255 mated by second-order central finite differences (for a derivation see, e.g., Cuvelier
 256 et al., 1986, section 2.2.1). The matrix rows repeat triples (-1,2,-1) to form a tridi-
 257 agonal symmetric matrix for which (very) efficient solution methods exist.

258 *Implementation* While writing out the system of equations is instructive and so-
 259 lutions can be constructed by manual Gaussian elimination for a small number of
 260 degrees of freedom n , solution of the equations governing subduction zone ther-
 261 mal structure requires significantly more involved code. Modern software design
 262 approaches have become available that allow us to develop numerical code using
 263 a relatively simple syntax in which the developer describes the problem in terms
 264 of the differential equation and boundary conditions, specifies the coefficients, the
 265 geometry and its discretization, and solution methods. We will provide a few exam-
 266 ples of high-level syntax (written in python) that can be used with the open-source
 267 FEniCS software (Logg et al., 2012) to produce a finite element code. We will first
 268 introduce this syntax and provide a more complete description of the approach that
 269 we use in section 2.2.3.

```
270 # Import the dolfin library (a component of FEniCS)
271 from dolfin import *
272 def solve_poisson_1d(ne, p=1):
273     """
```

1
2
3
4

```

274 A python function to solve a one-dimensional Poisson problem
275 on a unit interval domain.
276 Parameters:
277     * ne - number of elements
278     * p - polynomial order of the solution function space
279 """
280 # Describe the domain (a one-dimensional unit interval)
281 # and also the tessellation of that domain into ne
282 # equally spaced elements
283 mesh = UnitIntervalMesh(ne)
284 # Define the solution function space using Lagrange polynomials
285 # of order p
286 V = FunctionSpace(mesh, "Lagrange", p)
287
288 # Define the trial and test functions on the same function space (V)
289 T_a = TrialFunction(V)
290 T_t = TestFunction(V)
291
292 # Define the location of the boundary, x=0
293 def boundary(x):
294     return x[0] < DOLFIN_EPS
295 # Specify the value and define a boundary condition (bc)
296 gD = Constant(0.0)
297 bc = DirichletBC(V, gD, boundary)
298
299 # Define the right hand side function, rhsf
300 x = SpatialCoordinate(mesh)
301 rhsf = (pi**2)*sin(pi*x[0]/2)/4
302
303 # Define the integral to be assembled into the stiffness matrix
304 S = inner(grad(T_t), grad(T_a))*dx
305 # Define the integral to be assembled into the forcing vector
306 f = T_t*rhsf*dx
307
308 # Define the solution and compute it (given the boundary condition,
309 bc)
310 T_i = Function(V)
311 solve(S == f, T_i, bc)
312
313 # Save solution to disk in XDMF format
314 ofile = XDMFFile("poisson_{}_{}.xdmf".format(ne,p,))
315 ofile.write(T_i)
316 ofile.close()
317
318 # Return the solution
319 return T_i

```

Listing 1 FEniCS example for the 1D Poisson FEM solution (see XDMF.org for a description of the XDMF file format)

320 The one-dimensional heat diffusion problem (15)–(17) can be solved using FEniCS
321 with the python function `solve_poisson_1d` (listing 1). Lagrange polynomials (defined
322 by the keyword argument `p` on line 17, which defaults to 1). Test (τ_t) and trial (τ_a)
323 functions are defined on this function space, before being used to describe the in-
324 tegrals defining \mathbf{S} and \mathbf{f} . The Dirichlet boundary condition at $x=0$ is then declared
325 as `bc` before being passed to a function `solve` that assembles the matrix-vector sys-
326 tem, manipulates it to ensure satisfaction of the essential boundary condition, and
327 solves for τ_i , the function containing the vector of values of \tilde{T} at the DOFs T_j .
328 Finally the solution is returned.

329 *Higher order elements* We will use this simple example further to show that we
330 can construct shape functions of higher order that allow us to find solutions that
331 are (in general) more accurate with the same number of nodal points compared to

332 solutions with lower order shape functions. We will construct quadratic Lagrange
 333 shape functions on the elements as shown in Figure 1b. Note that each element now
 334 has an internal nodal point such the number of nodal points for the fixed number of
 335 elements increases by nearly a factor of two compared to the linear P1 function space
 336 (Figure 1a). Within an element e_i ($x_{i-1} \leq x \leq x_i$) there are three shape functions that
 337 are of quadratic form

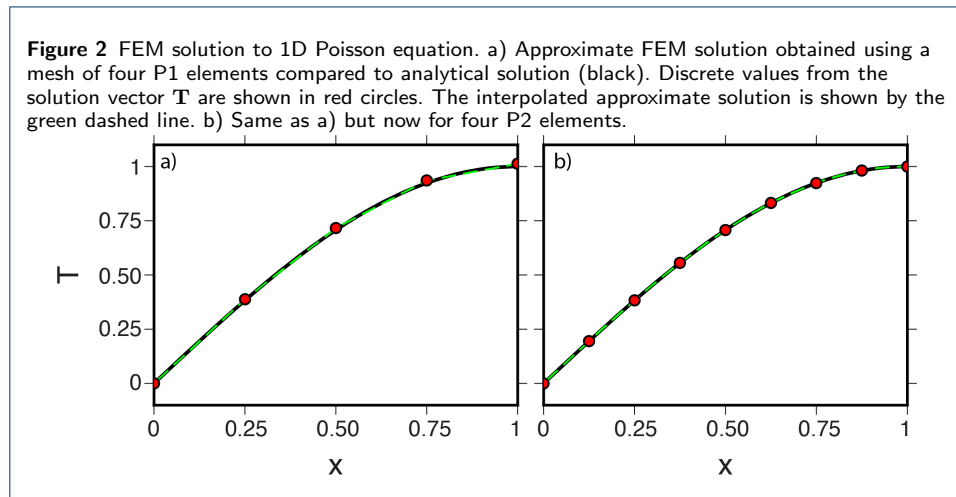
$$338 \quad \phi_{i-1} = \frac{2}{\Delta x^2}(x - x_i)(x - x_{i-1,i}) = 2\lambda_{i-1}(\lambda_{i-1} - \frac{1}{2}) \quad (29)$$

$$339 \quad \phi_{i-1,i} = \frac{-4}{\Delta x^2}(x - x_{i-1})(x - x_i) = 4\lambda_{i-1}\lambda_i \quad (30)$$

$$340 \quad \phi_i = \frac{2}{\Delta x^2}(x - x_{i-1})(x - x_{i-1,i}) = 2\lambda_i(\lambda_i - \frac{1}{2}) \quad (31)$$

342 with λ_i and λ_{i-1} defined in (25). We have used the notation $\phi_{i-1,i}$ to identify the
 343 internal Lagrange polynomial centered in element e_i on the new internal nodal point
 344 $x_{i-1,i}$. This also makes explicit the relation between the P1 nodal points and the
 345 edge nodal points (also called vertices) of the P2 elements and clarifies the relation
 346 between P1 and P2 shape functions through (29)–(31). Note that the nonzero values
 347 of a quadratic Lagrange shape function may extend beyond the neighboring DOFs
 348 and they can be positive or negative depending on where its nodal point is located
 349 within an element. Note also that the shape functions now connect more nodal
 350 points to the central nodal point – which suggests the matrix (28) changes form
 351 to have more entries per row than in the case of the P1 based matrix. In addition
 352 the matrix will have more rows since there are more nodal points for the same
 353 number of elements. Clearly the use of higher order elements comes at a greater
 354 computational cost since it is more expensive to solve a larger algebraic system.

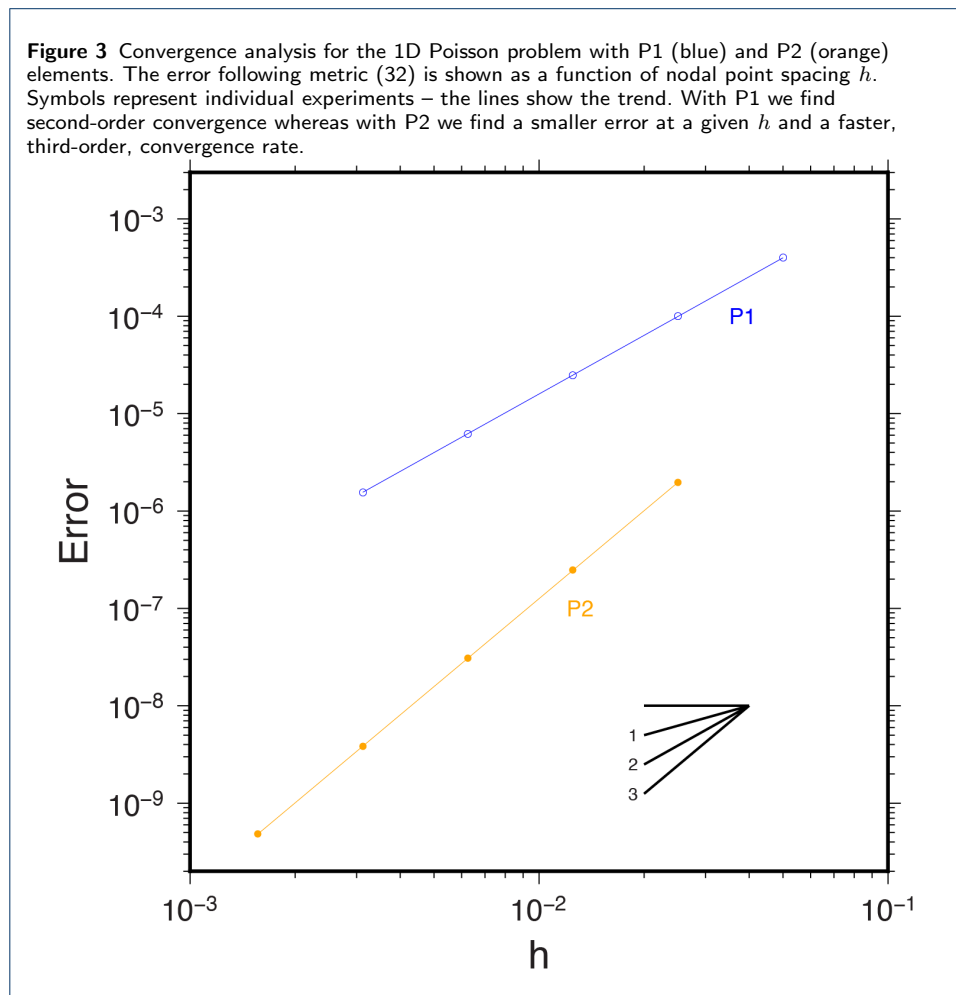
355 Calling the python function `solve_poisson_1d` with a second keyword argument
 356 `p=2` allows us to solve the system with quadratic Lagrange shape functions. The
 357 script shows that only the definition of the `FunctionSpace` is changed by setting `p=2`.
 358 Figure 2 shows the approximate solution for linear and quadratic elements on a
 359 coarse grid compared to the analytical solution. Note that the P2 solution stays
 closer to the analytical solution than the P1 solution.



361 *Convergence analysis* Repeating the numerical experiments with increasing n_e al-
 362 lows us to test the convergence of our approximate finite element solution to the
 363 known analytical solution (18). A key feature of any discretization technique is that
 364 with an increasing number of DOFs these solutions should converge, i.e. the error
 365 in our approximation should decrease. As an error metric we will use the L^2 norm
 366 of the difference between the approximate, \tilde{T} , and analytical, T , solutions

$$367 \quad e_{L^2,P} = \sqrt{\int_{\Omega} (\tilde{T} - T)^2 dx} \quad (32)$$

368 where the subscript P stands for Poisson. The rate at which this decreases is known
 369 as the order of convergence. Numerical analysis predicts a certain order depending
 370 on the type of the polynomials used as finite element shape functions and other
 371 constraints related to the well-posedness of the problem. For piecewise linear shape
 372 functions we expect second-order convergence, that is that the error decreases as
 373 h^{-2} where h is the nodal point spacing. With piecewise quadratic elements we
 374 expect to see third-order convergence. These expectations are met by the actual
 numerical experiments (Figure 3). Convergence analysis is an essential way to test



376 the accuracy of a numerical model but it relies on having a known analytical solution
377 and the ability to represent it and its boundary conditions in a discrete function
378 space. We will discuss this issue in the context of other examples with increasing
379 complexity below.

380 *2.2.3 Practical approaches, software availability, and comparison*

381 Traditionally, finite element methods have been implemented using Fortran or
382 C/C++ based codes that, at the core, build the matrix-vector system (8) by
383 numerical integration of (9) and (10) after which this system is solved by linear
384 algebraic solvers. Most FEM codes provide options for time-dependence and the
385 ability to solve nonlinear and nonlinearly coupled systems of PDEs. Examples of
386 such codes that have been used in geodynamical applications including subduction
387 zone modeling are ConMan (King et al., 1990), Sopale (Fullsack, 1995), Under-
388 world (Moresi et al., 2007), CitcomS (Zhong et al., 2008), MILAMIN (Dabrowski
389 et al., 2008), ASPECT (Kronbichler et al., 2013), Sepran (van den Berg et al.,
390 2015), Fluidity (Davies et al., 2011), and Rhea (Burstedde et al., 2013). A num-
391 ber of these are distributed as open-source software and many among those are
392 currently maintained through the Computational Infrastructure for Geodynamics
393 (geodynamics.org). These implementations can be shown to be accurate using in-
394 tercomparisons and benchmarks (e.g., Davies et al., 2011; Euen et al., 2022; King
395 et al., 2010; van Keken et al., 2008) and make use of advances in parallel computing
396 and efficient linear algebra solver techniques. Yet, modifications to the existing code
397 requires deep insight into the structure of the Fortran/C/C++ code which is not
398 trivial for experienced, let alone beginning, users.

399 In recent years an alternative approach for FEM has become available which el-
400 evates the user interface to simply specifying the FEM problem and solution method
401 with the high-level approach of which an example is shown in listing 1. The python
402 code is used to automatically build a finite element model that can be executed in
403 a variety of environments ranging from Jupyter notebooks (jupyter.org) and desk-
404 top computers to massively parallel high performance computers. Two prominent
405 examples of this approach are Firedrake (www.firedrakeproject.org) and FEniCS
406 (www.fenicsproject.org). Examples of the use of these two approaches in geody-
407 namical applications are in Davies et al. (2022) and Vynnytska et al. (2013).

408 We will focus on the use of the FEniCS (“Finite Elements in Computational
409 Sciences”; Alnæs et al., 2015) approach to solving FEM element equations. FEniCS
410 is a suite of open-source numerical libraries for the description of finite element
411 problems. Most importantly it provides a high-level, human-readable language for
412 the description of equations in python (the “Unified Form Language” (UFL); Alnæs
413 et al., 2014, an example of which we provided in listing 1) and a compiler (the “FEn-
414 iCS Form Compiler” (FFC); Kirby and Logg, 2006) to write fast code to assemble
415 the resulting discrete matrix-vector system. We will specifically use FEniCS within
416 TerraFERMA (the “Transparent Finite Element Rapid Model Assembler”; Wilson
417 et al., 2017). TerraFERMA provides a graphical user interface (using the “System
418 for Problem Description” (SPuD); Ham et al., 2009) that allows users to describe
419 the geometry, variables, and boundary conditions of their problem and construct
420 physics-based solvers using PETSc (the “Portable Extensible Toolkit for Scientific
421 computation”; Balay et al., 2023).

422 TerraFERMA aims to increase transparency in modeling by exposing all op-
 423 tions, including the equations, in a single options file that can be validated and
 424 automatically updated, which increases reproducibility. We provide all options files
 425 used in the following sections in a repository and in a docker image (see Supple-
 426 mentary Information) for readers to try. In addition to results from TerraFERMA
 427 we compare some solutions with the aforementioned finite element package Sepran
 428 which has been used extensively in subduction zone modeling (e.g., Syracuse et al.,
 429 2010; van Keken et al., 2011). Sepran is not an open-source code but allows for
 430 direct comparisons between independent finite element methods and establish their
 431 relative precision.

432 2.2.4 The Poisson equation beyond 1D

433 We can generalize (and formalize) the description of the Poisson equation using the
 434 steady-state heat diffusion equation in multiple dimensions, where (14) becomes

$$435 \quad -\nabla \cdot (k\nabla T) = H \quad \text{in } \Omega \quad (33)$$

437 after assuming zero velocity. T is the temperature solution we are seeking, k is
 438 the thermal conductivity and H is a heat source. If k is constant in space we can
 439 simplify (33) to

$$440 \quad -\nabla^2 T = f \quad \text{in } \Omega \quad (34)$$

442 where $f = \frac{H}{k}$.

443 *Boundary conditions* We supplement (34) with some combination of the boundary
 444 conditions (2)

$$445 \quad T = g_D \quad \text{on } \partial\Omega_D \subset \partial\Omega \quad (35)$$

$$446 \quad \nabla T \cdot \hat{n} = g_N \quad \text{on } \partial\Omega_N \subset \partial\Omega \quad (36)$$

$$447 \quad aT + \nabla T \cdot \hat{n} = g_R \quad \text{on } \partial\Omega_R \subset \partial\Omega \quad (37)$$

449 where $\partial\Omega_D$, $\partial\Omega_N$ and $\partial\Omega_R$ are segments of the domain boundary that do not
 450 overlap ($\partial\Omega_D \cap \partial\Omega_N = \emptyset$, $\partial\Omega_D \cap \partial\Omega_R = \emptyset$, $\partial\Omega_N \cap \partial\Omega_R = \emptyset$) and that together
 451 span the entire boundary ($\partial\Omega_D \cup \partial\Omega_N \cup \partial\Omega_R = \partial\Omega$). The unit outward-pointing
 452 normal to the boundary $\partial\Omega$ is denoted by \hat{n} and $g_D = g_D(\vec{x}, t)$, $g_N = g_N(\vec{x}, t)$
 453 and $g_R = g_R(\vec{x}, t)$ are known functions of space and time. Equation (35) is known
 454 as a Dirichlet boundary condition and specifies the value of the solution on $\partial\Omega_D$.
 455 Equation (36) is a Neumann boundary condition and specifies the value of the flux
 456 through $\partial\Omega_N$. Finally, equation (37) is a Robin boundary condition, which describes
 457 a linear combination of the flux and the solution on $\partial\Omega_R$.

458 *Weak form* The first step in the finite element discretization of (34) is to transform
 459 it into its weak form. Following (7), this requires multiplying the equation by a test
 460 function, T_t , and integrating over the domain Ω

$$461 \quad - \int_{\Omega} T_t \nabla^2 T \, dx = \int_{\Omega} T_t f \, dx \quad (38)$$

462 After integrating the left-hand side by parts

$$463 \quad \int_{\Omega} \nabla T_t \cdot \nabla T \, dx - \int_{\partial\Omega} T_t \nabla T \cdot \hat{n} \, ds = \int_{\Omega} T_t f \, dx \quad (39)$$

464 we can see that we have reduced the continuity requirements on T by only requiring
 465 its first derivative to be bounded across Ω (see Hughes, 1987, for a more formal
 466 discussion of the requirements on the solution). Integrating by parts also allows
 467 Neumann and Robin boundary conditions to be imposed “naturally” through the
 468 second integral on the left-hand side since this directly incorporates the flux com-
 469 ponents across the boundary. In this formulation, Dirichlet conditions cannot be
 470 imposed weakly and are referred to as essential boundary conditions, that are re-
 471 quired of the solution but do not arise naturally in the weak form. The weak form
 472 therefore becomes: find T such that $T = g_D$ on $\partial\Omega_D$ and

$$473 \quad \int_{\Omega} \nabla T_t \cdot \nabla T \, dx - \int_{\partial\Omega_N} T_t g_N \, ds - \int_{\partial\Omega_R} T_t (g_R - aT) \, ds = \int_{\Omega} T_t f \, dx \quad (40)$$

474 for all T_t such that $T_t = 0$ on $\partial\Omega_D$.

475 *Discretization* The weak (40) and strong (34)–(37) forms of the problem are equiv-
 476 alent so long as the solution is sufficiently smooth. We make our first approximation
 477 to the solution by seeking the trial function \tilde{T} such that $\tilde{T} = g_D$ on $\partial\Omega_D$ where

$$478 \quad T \approx \tilde{T} = \sum_j \phi_j T_j \quad (41)$$

479 for all test functions \tilde{T}_t where

$$480 \quad T_t \approx \tilde{T}_t = \sum_i \phi_i T_{ti} \quad (42)$$

481 noting again that $\tilde{T}_t = 0$ on $\partial\Omega_D$. The finite element shape functions ϕ_j are as
 482 discussed earlier. Assuming these are continuous across elements of the mesh, (41)
 483 and (42) can be substituted into (40) to yield

$$484 \quad \begin{aligned} 485 \quad & \sum_i \sum_j T_{ti} T_j \sum_k \int_{e_k} \nabla \phi_i \cdot \nabla \phi_j \, dx + \sum_i \sum_j T_{ti} T_j \sum_k \int_{\partial e_k \cap \partial\Omega_R} \phi_i a \phi_j \, ds \\ 486 \quad & - \sum_i T_{ti} \sum_k \int_{\partial e_k \cap \partial\Omega_N} \phi_i g_N \, ds - \sum_i T_{ti} \sum_k \int_{\partial e_k \cap \partial\Omega_R} \phi_i g_R \\ 487 \quad & = \sum_i T_{ti} \sum_k \int_{e_k} \phi_i f \, dx \quad (43) \\ 488 \end{aligned}$$

489 where we are integrating over the whole domain by summing the integrals over
 490 all the elements e_k ($\int_{\Omega} dx = \sum_k \int_{e_k} dx$). Note that in practice, because the shape
 491 functions are zero over most of the domain, only element integrals with non-zero
 492 values need be included in the summation. The element boundaries, ∂e_k , are only of
 493 interest (due to the assumed continuity of the shape functions between the elements)

494 if they either intersect with $\partial\Omega_N$, $\partial e_k \cap \partial\Omega_N$, or $\partial\Omega_R$, $\partial e_k \cap \partial\Omega_R$. Since the solution
 495 of the now discretized weak form should be valid for all \tilde{T}_t we can drop T_{ti} from
 496 (43)

$$\begin{aligned}
 & \sum_j T_j \sum_k \int_{e_k} \nabla \phi_i \cdot \nabla \phi_j \, dx + \sum_j T_j \sum_k \int_{\partial e_k \cap \partial\Omega_R} \phi_i a \phi_j \, ds \\
 & - \sum_k \int_{\partial e_k \cap \partial\Omega_N} \phi_i g_N \, ds - \sum_k \int_{\partial e_k \cap \partial\Omega_R} \phi_i g_R \, ds = \sum_k \int_{e_k} \phi_i f \, dx \quad (44)
 \end{aligned}$$

501 This represents a matrix-vector system of the form of (8) with

$$\mathbf{S} = S_{ij} = \sum_k \int_{e_k} \nabla \phi_i \cdot \nabla \phi_j \, dx + \sum_k \int_{\partial e_k \cap \partial\Omega_R} \phi_i a \phi_j \, ds \quad (45)$$

$$\mathbf{f} = f_i = \sum_k \int_{e_k} \phi_i f \, dx + \sum_k \int_{\partial e_k \cap \partial\Omega_N} \phi_i g_N \, ds + \sum_k \int_{\partial e_k \cap \partial\Omega_R} \phi_i g_R \, ds \quad (46)$$

$$\mathbf{u} = \mathbf{T} = T_j \quad (47)$$

506 The compact support of the shape functions $\phi_{(i,j)}$, which limits their nonzero values
 507 to the elements immediately neighboring DOF i or j , means that the integrals in
 508 (45)–(46) can be evaluated efficiently by only considering shape functions associated
 509 with an element e_k . It also means that the resulting matrix \mathbf{S} is sparse, with most
 510 entries being zero. These properties can be seen by considering a one-dimensional
 511 version of (34) as discussed in section 2.2.2.

512 For an example of the implementation of the 2D Poisson problem on a unit
 513 square see listing 2 with convergence tests and solution in Figure 4. In this case we
 514 use a manufactured solution (that is, one that is not necessarily an example of a
 515 solution to a PDE representing a naturally occurring physical problem) where we
 516 take a known analytical solution $T(x, y)$ and substitute this into (34) to find f , then
 517 use this as the right-hand side in our numerical test. We choose $T(x, y) = \exp(x + \frac{y}{2})$
 518 which is the solution to

$$-\nabla^2 T = -\frac{5}{4} \exp(x + \frac{y}{2}) \quad (48)$$

520 Solving (48) numerically in a unit square, $\Omega = [0, 1] \times [0, 1]$, for the approximate
 521 solution $\tilde{T} \approx T$, we impose the boundary conditions

$$\tilde{T} = \exp(x + \frac{y}{2}) \quad \text{on } \partial\Omega \text{ where } x = 0 \text{ or } y = 0 \quad (49)$$

$$\nabla \tilde{T} \cdot \hat{n} = \exp(x + \frac{y}{2}) \quad \text{on } \partial\Omega \text{ where } x = 1 \quad (50)$$

$$\nabla \tilde{T} \cdot \hat{n} = \frac{1}{2} \exp(x + \frac{y}{2}) \quad \text{on } \partial\Omega \text{ where } y = 1 \quad (51)$$

526 where (49) represents an essential Dirichlet condition on the value of \tilde{T} and (50)–
 527 (51) are natural Neumann conditions on $\nabla \tilde{T}$.

528 Listing 2 shows an implementation of this problem using FEniCS, which returns
 529 the approximate solution \tilde{T} . Comparison of this to the analytical solution T using

530 the metric (32) gives the expected order of convergence for the P1 and P2 elements
 531 (see Figure 4).

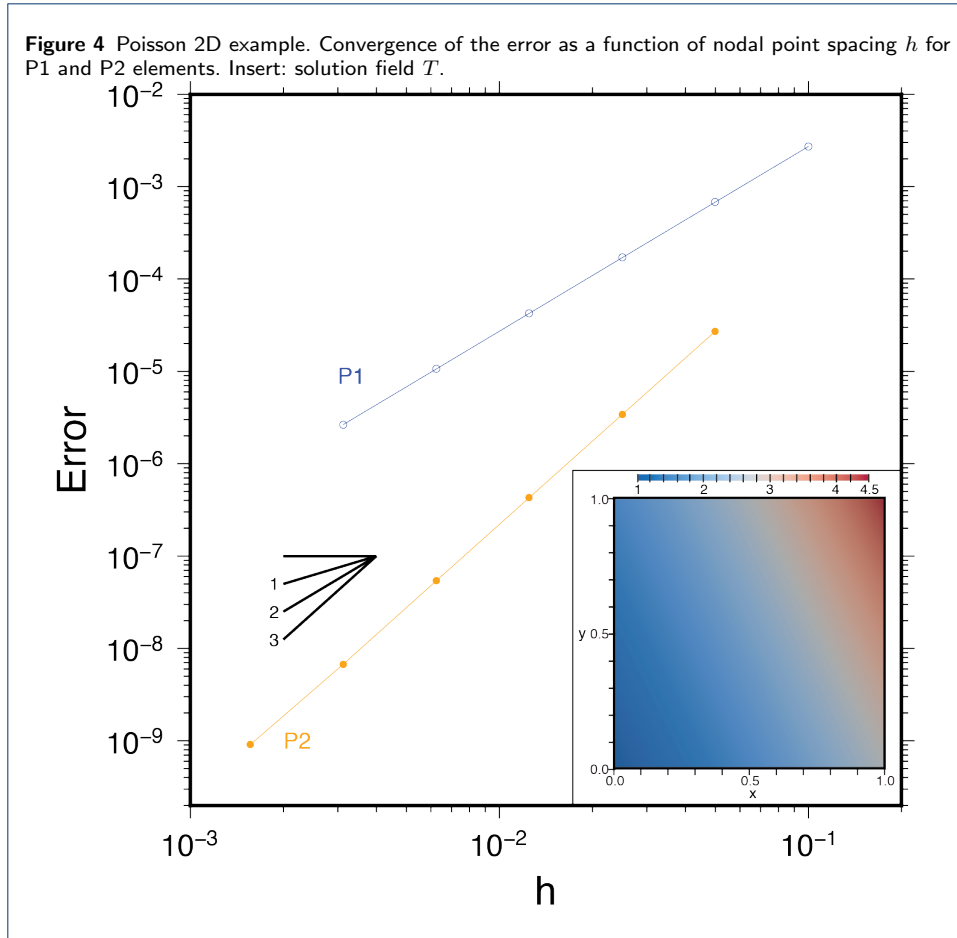
```

532 from dolfin import *
533 def solve_poisson_2d(ne, p=1):
534     """
535     A python function to solve a two-dimensional Poisson problem
536     on a unit square domain.
537     Parameters:
538     * ne - number of elements in each dimension
539     * p - polynomial order of the solution function space
540     """
541     # Describe the domain (a unit square)
542     # and also the tessellation of that domain into ne
543     # equally spaced squares in each dimension which are
544     # subdivided into two triangular elements each
545     mesh = UnitSquareMesh(ne, ne, diagonal='right')
546     # Define the solution function space using Lagrange polynomials
547     # of order p
548     V = FunctionSpace(mesh, "Lagrange", p)
549
550     # Define the trial and test functions on the same function space (V)
551     T_a = TrialFunction(V)
552     T_t = TestFunction(V)
553
554     # Define the location of the boundary condition, x=0 and y=0
555     def boundary(x):
556         return x[0] < DOLFIN_EPS or x[1] < DOLFIN_EPS
557     # Specify the value and define a Dirichlet boundary condition (bc)
558     gD = Expression("exp(x[0] + x[1]/2.)", degree=p)
559     bc = DirichletBC(V, gD, boundary)
560
561     # Get the coordinates
562     x = SpatialCoordinate(mesh)
563     # Define the Neumann boundary condition function
564     gN = as_vector((exp(x[0] + x[1]/2.), 0.5*exp(x[0] + x[1]/2.)))
565     # Define the right hand side function, rhsf
566     rhsf = -5./4.*exp(x[0] + x[1]/2.)
567
568     # Get the unit vector normal to the facets
569     n = FacetNormal(mesh)
570     # Define the integral to be assembled into the stiffness matrix
571     S = inner(grad(T_t), grad(T_a))*dx
572     # Define the integral to be assembled into the forcing vector,
573     # incorporating the Neumann boundary condition weakly
574     f = T_t*rhsf*dx + T_t*inner(gN, n)*ds
575
576     # Define the solution and compute it (given the boundary condition,
577     # bc)
578     T_i = Function(V)
579     solve(S == f, T_i, bc)
580
581     # Save solution to disk in XDMF format
582     ofile = XDMFFile("poisson_{_}.xmf".format(ne,p))
583     ofile.write(T_i)
584     ofile.close()
585
586     # Return the solution
587     return T_i
  
```

Listing 2 FEniCS script for 2D Poisson problem

588 2.2.5 Batchelor cornerflow problem

589 The solid flow in a subduction zone is primarily driven by the motion of the down-
 590 going slab entraining material in the mantle wedge and dragging it down with it
 591 setting up a cornerflow in the mantle wedge (see, e.g., Figure 1a in part I). This



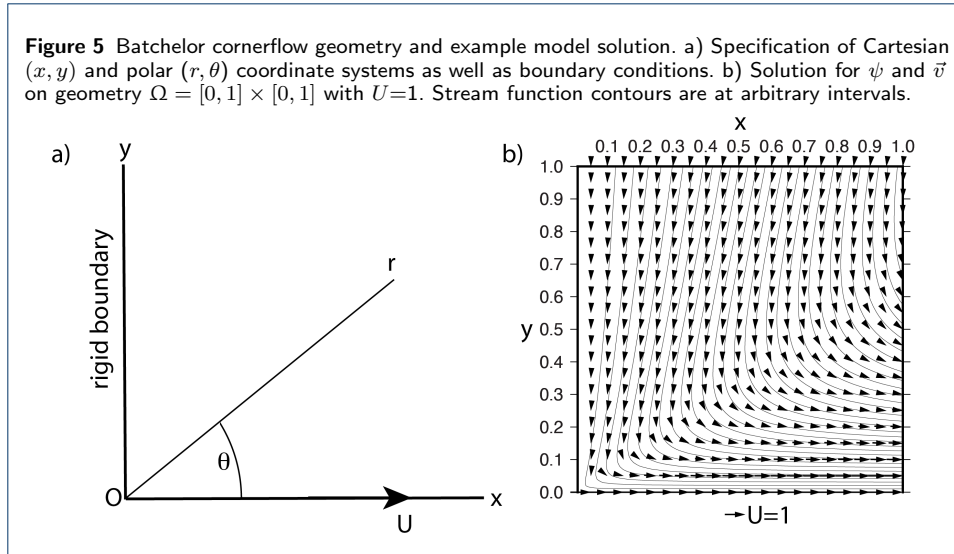
592 effect can be simulated by imposing the motion of the slab as a kinematic boundary
 593 condition at the base of the dynamic mantle wedge, allowing us to drop the buoy-
 594 ancy term from (12), $\vec{f}_B=0$. With the further assumption of an isoviscous rheology,
 595 $2\eta=1$, the momentum and mass equations simplify to

$$596 \quad -\nabla \cdot \left(\frac{\nabla \vec{v} + \nabla \vec{v}^T}{2} \right) + \nabla P = 0 \quad \text{in } \Omega \quad (52)$$

$$597 \quad \nabla \cdot \vec{v} = 0 \quad \text{in } \Omega \quad (53)$$

599 Here, \vec{v} is the velocity of the mantle in the subduction zone wedge, Ω , and P is
 600 the pressure. Imposing isothermal conditions means that (14) has been dropped
 601 altogether. With these simplifications we can test our numerical solution to (52)–
 602 (53) against the analytical solution provided by Batchelor (1967).

603 *Analytical solution* To more easily describe the analytical solution, we consider
 604 the cornerflow geometry in Figure 5a where we have rotated the mantle wedge by
 605 90° counterclockwise and assumed a 90° angle between the wedge boundaries. In
 606 this geometry Equations (52)–(53) can be transformed into a biharmonic equation



607 for the stream function, ψ ,

$$608 \quad \nabla^4 \psi = 0 \quad (54)$$

609 where $\psi = \psi(r, \theta)$ is a function of the radius, r , and angle from the x -axis, θ , related
610 to the velocity, $\vec{v} = \vec{v}(x, y)$ by

$$611 \quad \vec{v} = \begin{pmatrix} \cos \theta & -\sin \theta \\ \sin \theta & \cos \theta \end{pmatrix} \begin{pmatrix} \frac{1}{r} \frac{\partial \psi}{\partial \theta} \\ -\frac{\partial \psi}{\partial r} \end{pmatrix} \quad (55)$$

613 With semi-infinite x and y axes, a rigid boundary condition, $\vec{v} = \vec{0}$, along the
614 y -axis (the rotated “crust” at the top of the wedge), and a kinematic boundary
615 condition on the x -axis (the “slab” surface at the base of the wedge), $\vec{v} = (U, 0)^T$,
616 the analytical solution is found as

$$617 \quad \psi(r, \theta) = \frac{rU}{\frac{1}{4}\pi^2 - 1} \left(-\frac{1}{4}\pi^2 \sin \theta + \frac{1}{2}\pi\theta \sin \theta + \theta \cos \theta \right) \quad (56)$$

618 *Discretization* Since it is not possible with our numerical approach to solve the
619 equations in a semi-infinite domain, we discretize (52)–(53) in a unit square domain
620 with unit length in the x and y domains, as in Figure 5b. We choose different function
621 spaces, with different shape functions, $\vec{\omega}_j(x)$ and $\chi_j(x)$ for the approximations
622 of \vec{v} and P respectively, such that

$$623 \quad \vec{v} \approx \vec{\tilde{v}} = \sum_j \omega_j^k v_j^k \quad (57)$$

$$624 \quad P \approx \tilde{P} = \sum_j \chi_j P_j \quad (58)$$

626 where v_j^k and P_j are the values of velocity and pressure at node j respectively and
627 the superscript k represents the spatial component of \vec{v} . The discrete test functions

628 \tilde{v}_t and \tilde{P}_t are similarly defined. We will discuss the choice of $\vec{\omega}_j = \omega_j^k$ and χ_j later
 629 but simply assume that they are continuous across elements of the mesh in the
 630 following.

631 *Boundary conditions* To match the analytical solution (56) we apply essential
 632 Dirichlet conditions on \tilde{v} on all four sides of the domain

$$633 \quad \tilde{v} = (0, 0)^T \quad \text{on } \partial\Omega \text{ where } x = 0 \quad (59)$$

$$634 \quad \tilde{v} = (U, 0)^T \quad \text{on } \partial\Omega \text{ where } y = 0 \quad (60)$$

$$635 \quad \tilde{v} = \vec{v} \quad \text{on } \partial\Omega \text{ where } x = 1 \text{ or } y = 1 \quad (61)$$

637 Note that the first two conditions imply a discontinuity in the solution for \tilde{v} at
 638 $(x, y) = (0, 0)$. The last boundary condition simply states that we apply the analyti-
 639 cal solution (obtained from (56) via (55)) at the boundaries at $x=1$ and $y=1$. One
 640 consequence of applying essential boundary conditions on \vec{v} on all sides of the do-
 641 main is that P is unconstrained up to a constant value as only its spatial derivatives
 642 appear in the equations. The ability to add an arbitrary constant to the pressure
 643 is referred to as the pressure containing a null space. This makes it impossible to
 644 find a unique solution to (52)–(53) with (59)–(61) since an infinite number of pres-
 645 sure solutions exist. There are a number of ways to select an appropriate pressure
 646 solution. Here we arbitrarily choose one such solution by adding the condition that

$$647 \quad \tilde{P} = 0 \quad \text{at } (x, y) = (0, 0) \quad (62)$$

649 which will allow a unique solution to the discrete equations to be found.

650 *Weak form* Multiplying (52) by \vec{v}_t and (53) by P_t , integrating (by parts) over Ω ,
 651 and discretizing the test and trial functions allows the discrete matrix-vector system
 652 of the form of (8) to be written as

$$653 \quad \mathbf{S} = \begin{pmatrix} \mathbf{K} & \mathbf{G} \\ \mathbf{D} & \mathbf{0} \end{pmatrix} \quad (63)$$

$$654 \quad \mathbf{K} = K_{i_1 j_1} = \sum_k \int_{e_k} \left(\frac{\nabla \vec{\omega}_{i_1} + \nabla \vec{\omega}_{i_1}^T}{2} \right) : \left(\frac{\nabla \vec{\omega}_{j_1} + \nabla \vec{\omega}_{j_1}^T}{2} \right) dx \quad (64)$$

$$655 \quad \mathbf{G} = G_{i_1 j_2} = - \sum_k \int_{e_k} \nabla \cdot \vec{\omega}_{i_1} \chi_{j_2} dx \quad (65)$$

$$656 \quad \mathbf{D} = D_{i_2 j_1} = - \sum_k \int_{e_k} \chi_{i_2} \nabla \cdot \vec{\omega}_{j_1} dx \quad (66)$$

$$657 \quad \mathbf{u} = (\mathbf{v}, \mathbf{P})^T = (\vec{v}_{j_1}, P_{j_2})^T \quad (67)$$

$$658 \quad \mathbf{f} = f_i = 0 \quad (68)$$

660 Note that in (64)–(66) all surface integrals around $\partial\Omega$ arising from integration
 661 by parts have been dropped because the velocity solution is fully specified on all
 662 boundaries. Additionally, when integrating (64) by parts we have used the fact

663 that $\nabla \vec{\omega}_{i_1} : \left(\frac{\nabla \vec{\omega}_{j_1} + \nabla \vec{\omega}_{j_1}^T}{2} \right) = \left(\frac{\nabla \vec{\omega}_{i_1} + \nabla \vec{\omega}_{i_1}^T}{2} \right) : \left(\frac{\nabla \vec{\omega}_{j_1} + \nabla \vec{\omega}_{j_1}^T}{2} \right)$ to demonstrate the
 664 symmetry of \mathbf{K} . In fact, \mathbf{S} has been made symmetric by integrating the gradient of
 665 pressure term, ∇P , by parts in (65) and negating (53) in (66) such that $\mathbf{G} = \mathbf{D}^T$.
 666 This symmetry property can be exploited when choosing an efficient method of
 667 solving (8).

668 As before, the weak form of (63) may be described using UFL with rather
 669 simple python code shown in listing 3.

```
670 K = inner(sym(grad(v_t)), sym(grad(v_a))) * dx 1
671 G = -div(v_t) * p_a * dx 2
672 D = -p_t * div(v_a) * dx 3
673 S = K + G + D 4
```

Listing 3 Weak form of Stokes system

674 For the sake of brevity we have assumed that the test and trial functions v_t , p_t ,
 675 v_a and p_a have been declared. Additional code is also required to fully describe the
 676 boundary conditions and solve the resulting system. The full example is provided
 677 in the Supplementary Information as a TerraFERMA input file.

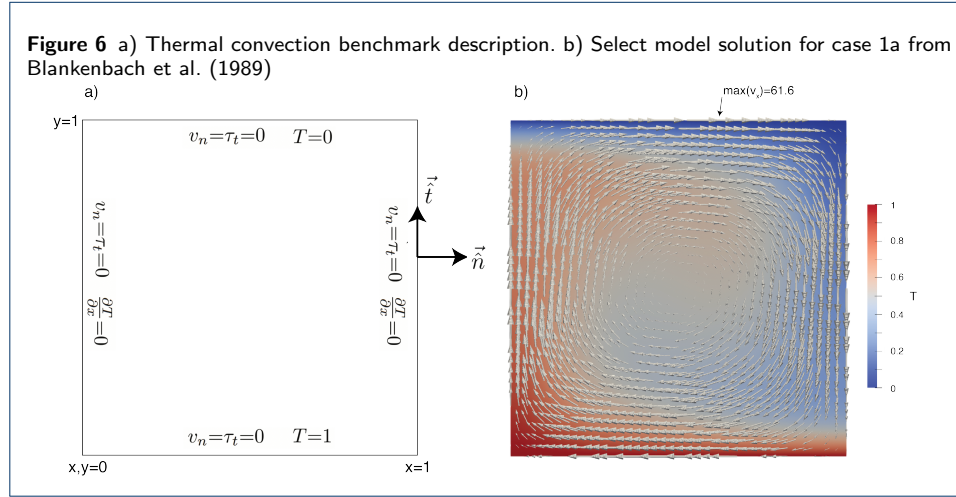
678 An important aspect of \mathbf{S} is that it describes a so-called “saddle point” system.
 679 The lower right block is zero, which indicates that pressure is acting in this system
 680 as a Lagrange multiplier, enforcing the constraint that the velocity is divergence
 681 free but not appearing in (53) itself. Such systems require special consideration
 682 of the choice of shape functions for the discrete approximations of velocity and
 683 pressure to ensure the stability of the solution, \mathbf{u} . Several choices of so-called stable
 684 element pairs, $(\vec{\omega}_j, \chi_j)$ are available in the literature (e.g., Auricchio et al., 2017).
 685 Here we select the frequently used lowest-order Taylor-Hood element pair, in which
 686 $\vec{\omega}_j$ are piecewise-quadratic and χ_j are piecewise-linear polynomials, referred to on
 687 triangular (and tetrahedral in 3D) meshes as P2P1. This fulfills a necessary (but not
 688 sufficient) criterion for stability that the velocity has more DOFs than the pressure.
 689 Solving (63)–(68) subject to the conditions (59)–(62) on a series of successively finer
 690 meshes and comparing the resulting solution to the analytical result given by (56)
 691 and (55) using the error metric

$$692 \quad e_{L^2, B} = \sqrt{\int_{\Omega} (\tilde{v} - \vec{v}) \cdot (\tilde{v} - \vec{v}) dx} \quad (69)$$

693 (where B stands for Batchelor) shows linear rather than quadratic convergence.
 694 We encourage the reader to convince themselves of this by running the example.
 695 This first-order convergence rate is lower than would be expected for piecewise
 696 quadratic velocity functions. This drop in convergence is caused by the boundary
 697 conditions at the origin being discontinuous, which cannot be represented in the
 698 selected function space and results in a pressure singularity at that point. This is
 699 an example where convergence analysis demonstrates suboptimal results due to our
 700 inability to represent the solution in the selected finite element function space.

701 *2.2.6 Blankenbach thermal convection benchmark*

702 Before discussing the solution of the full governing equations for subduction zone
 703 thermal structure we will explore solving the equations governing a buoyancy-driven
 704 convection model in a square domain following the steady-state mantle convection
 705 benchmarks from Blankenbach et al. (1989). This example allows us to couple a
 706 steady-state advection-diffusion equation for temperature to the Stokes and mass
 707 conservation equations we have already discussed. This also provides an example
 708 of solving a nonlinearly coupled system and will show how we can test a model for
 709 which no analytical solution exists.



710 The flow in the box is driven by heating from below and cooling from above
 711 (Figure 6). We solve (12)–(13)

$$712 \quad -\nabla \cdot \left(2\eta \frac{\nabla \vec{v} + \nabla \vec{v}^T}{2} \right) + \nabla P = -RaT\hat{g} \quad \text{in } \Omega \quad (70)$$

$$713 \quad \nabla \cdot \vec{v} = 0 \quad \text{in } \Omega \quad (71)$$

715 where variable rheology is permitted through the inclusion of the viscosity η and
 716 the buoyancy force vector has been defined as $\vec{f}_B = -RaT\hat{g}$, using the tempera-
 717 ture T , nondimensional Rayleigh number, Ra , and unit vector in the direction of
 718 gravity, \hat{g} . The Rayleigh number arises from the nondimensionalization of the gov-
 719 erning equations and is a ratio that balances factors that enhance convective vigor
 720 (e.g., thermal expansivity, gravity) with those that retard convective vigor (e.g.,
 721 viscosity). In general, convective vigor increases with increasing Ra when it exceeds
 722 a critical value for the Rayleigh number (see, e.g., Turcotte and Schubert, 2002).
 723 The heat equation (14), under the assumptions of steady state ($\frac{\partial T}{\partial t} = 0$), constant
 724 material properties ($k=1$), and zero internal heating ($H=0$) reads

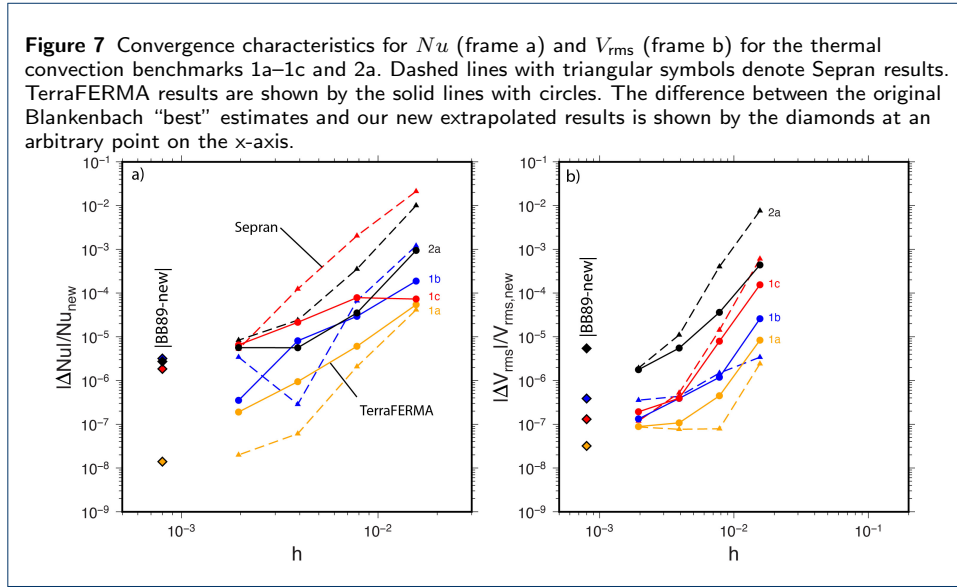
$$725 \quad \vec{v} \cdot \nabla T = \nabla^2 T \quad \text{in } \Omega \quad (72)$$

727 *Boundary conditions* We discretize the trial function spaces for temperature
 728 ($T \approx \tilde{T}$), velocity ($\vec{v} \approx \tilde{\vec{v}}$), and pressure ($P \approx \tilde{P}$) as before using (41), (57) and (58),

729 with similarly defined discrete test functions, \tilde{T}_t , \tilde{v}_t and \tilde{P}_t . For the Stokes problem
 730 we assume free-slip boundaries. These are formed by the combination of a Dirichlet
 731 boundary condition of zero normal velocity ($v_n = \tilde{v} \cdot \hat{n} = 0$) and a Neumann zero tan-
 732 gential stress condition ($\tau_t = (\boldsymbol{\tau} \cdot \hat{n}) \cdot \hat{t} = 0$). Here, \hat{n} is the unit normal to the boundary,
 733 \hat{t} is the unit tangent on the boundary (see Figure 6a), and $\boldsymbol{\tau}$ is the deviatoric stress
 734 tensor

$$735 \quad \boldsymbol{\tau} = 2\eta \frac{\nabla \tilde{\boldsymbol{v}} + \nabla \tilde{\boldsymbol{v}}^T}{2} = 2\eta \begin{bmatrix} \frac{\partial \tilde{v}_x}{\partial x} & \frac{1}{2} \left(\frac{\partial \tilde{v}_x}{\partial y} + \frac{\partial \tilde{v}_y}{\partial x} \right) \\ \frac{1}{2} \left(\frac{\partial \tilde{v}_x}{\partial y} + \frac{\partial \tilde{v}_y}{\partial x} \right) & \frac{\partial \tilde{v}_y}{\partial y} \end{bmatrix} \quad (73)$$

736 This set of velocity boundary conditions once again results in a pressure null space.
 737 We arbitrarily choose to impose the extra condition that $\tilde{P}(0, 0) = 0$ to force a unique
 738 solution to exist. For the heat equation the side boundaries are insulating (imposed
 739 by the Neumann boundary condition $\partial \tilde{T} / \partial x = 0$) with Dirichlet boundary conditions
 740 for the top boundary ($\tilde{T} = 0$) and bottom boundary ($\tilde{T} = 1$).



741 *Nonlinearity* Unlike the previous examples, which were linear problems of their
 742 solution variables, (70)–(72) are nonlinear. For an isoviscous rheology the equations
 743 are individually linear but the buoyancy contribution to (70) and the advective
 744 component in (72) mean that the coupled system of equations is nonlinear, with
 745 $\tilde{\boldsymbol{v}}$ depending on T and vice versa. For non-Newtonian rheologies, where $\eta = \eta(\tilde{\boldsymbol{v}})$,
 746 (70) itself becomes nonlinear too. Because of this, rather than immediately defining
 747 the weak forms of the linear operator \mathbf{S} we begin by considering the weak form
 748 of the nonlinear residual, \mathbf{r} . This is derived in exactly the same manner as before
 749 by multiplying (70) by \tilde{v}_t , (71) by P_t and (72) by T_t , discretizing the functions,
 750 integrating (by parts) over the domain Ω , dropping the resulting surface integrals
 751 (either to enforce the weak boundary conditions or because they are unnecessary

752 due to the essential boundary conditions), and defining the discrete weak forms as

$$753 \quad \mathbf{r}_{\tilde{v}} = r_{\tilde{v}_{i_1}} := \sum_k \int_{e_k} \left[\left(\frac{\nabla \tilde{\omega}_{i_1} + \nabla \tilde{\omega}_{i_1}^T}{2} \right) : 2\eta \left(\frac{\nabla \tilde{v} + \nabla \tilde{v}^T}{2} \right) - \nabla \cdot \tilde{\omega}_{i_1} \tilde{P} + \tilde{\omega}_{i_1} \cdot \tilde{g} Ra \tilde{T} \right] dx = 0 \quad (74)$$

$$754 \quad \mathbf{r}_P = r_{P_{i_2}} := - \sum_k \int_{e_k} \chi_{i_2} \nabla \cdot \tilde{v} dx = 0 \quad (75)$$

$$755 \quad \mathbf{r}_T = r_{T_{i_3}} := \sum_k \int_{e_k} \left[\phi_{i_3} \tilde{v} \cdot \nabla \tilde{T} + \nabla \phi_{i_3} \cdot \nabla \tilde{T} \right] dx = 0 \quad (76)$$

757 Here $\mathbf{r} = (\mathbf{r}_{\tilde{v}}, \mathbf{r}_P, \mathbf{r}_T)^T = (r_{\tilde{v}_{i_1}}, r_{P_{i_2}}, r_{T_{i_3}})^T$ is a residual vector, the root of which
 758 must be found in order to find an approximate solution to (70)–(72). Finding the
 759 exact root is not generally possible. Instead we aim to find $\mathbf{r} = \mathbf{0}$ within some toler-
 760 ance. For example we can use an L^2 norm and an absolute $\|\mathbf{r}\|_2 = \sqrt{\mathbf{r} \cdot \mathbf{r}} < \epsilon_{\text{atol}}$,
 761 or relative, $\frac{\|\mathbf{r}\|_2}{\|\mathbf{r}^0\|_2} = \frac{\sqrt{\mathbf{r} \cdot \mathbf{r}}}{\sqrt{\mathbf{r}^0 \cdot \mathbf{r}^0}} < \epsilon_{\text{rtol}}$, tolerance, where \mathbf{r}^0 is the residual evaluated
 762 using the initial guess at the solution. We will briefly discuss two commonly used
 763 approaches to approximately finding the residual root.

764 *Newton's method* To find the root, $\mathbf{u}^{i+1} = (\mathbf{v}^{i+1}, \mathbf{P}^{i+1}, \mathbf{T}^{i+1})^T = (\tilde{v}_{j_1}^{i+1}, P_{j_2}^{i+1}, T_{j_3}^{i+1})^T$,
 765 we can expand the residual in a Taylor series around the current best guess at the
 766 solution $\mathbf{u}^i = (\mathbf{v}^i, \mathbf{P}^i, \mathbf{T}^i)^T = (\tilde{v}_{j_1}^i, P_{j_2}^i, T_{j_3}^i)^T$ such that

$$767 \quad \mathbf{r}(\mathbf{u}^{i+1}) = \mathbf{r}(\mathbf{u}^i) + \mathbf{r}'(\mathbf{u}^i) (\mathbf{u}^{i+1} - \mathbf{u}^i) + \mathbf{r}''(\mathbf{u}^i) (\mathbf{u}^{i+1} - \mathbf{u}^i)^2 + \dots = \mathbf{0} \quad (77)$$

768 where $\mathbf{r}'(\mathbf{u}^i)$ and $\mathbf{r}''(\mathbf{u}^i)$ represent the first and second order derivatives of the
 769 residual with respect to the solution variables, evaluated at \mathbf{u}^i . Dropping terms with
 770 orders higher than first, defining the Jacobian $\mathbf{J}(\mathbf{u}^i) = \mathbf{r}'(\mathbf{u}^i)$ and $\delta \mathbf{u} = \mathbf{u}^{i+1} - \mathbf{u}^i$,
 771 and rearranging results in the matrix equation

$$772 \quad \mathbf{J}(\mathbf{u}^i) \delta \mathbf{u} = -\mathbf{r}(\mathbf{u}^i) \quad (78)$$

773 which can be solved for $\delta \mathbf{u}$ and used to find $\mathbf{u}^{i+1} = \mathbf{u}^i + \delta \mathbf{u}$. Since we have dropped
 774 terms from the Taylor expansion \mathbf{u}^{i+1} will only be a first-order approximation of
 775 the root of \mathbf{r} . So long as the initial guess \mathbf{u}^i is close enough to the final solution
 776 and (78) is solvable then \mathbf{u}^{i+1} should give a better estimate of $\mathbf{r} = \mathbf{0}$, in the sense
 777 that $\mathbf{r}(\mathbf{u}^{i+1}) < \mathbf{r}(\mathbf{u}^i)$. Repeatedly solving (78) and at each iteration updating
 778 $\mathbf{u}^{i+1} \rightarrow \mathbf{u}^i$ will then result in a final solution where \mathbf{r} approaches $\mathbf{0}$ in some norm
 779 and to some tolerance.

780 For highly nonlinear problems the Jacobian matrix, $\mathbf{J} = \mathbf{r}'$, can be complicated
 781 and difficult to derive, let alone to code. Fortunately, modern finite element libraries,
 782 like FEniCS, that provide the symbolic and human-readable representation of weak
 783 forms seen above through UFL allow the Jacobian to be automatically evaluated
 784 and assembled. For (74)–(76) this results in the code snippet in listing 4.

```
785 rv = (inner(sym(grad(v_t)), 2*eta*sym(grad(v_i))) - div(v_t)*p_i \
786       + inner(v_t, gravity)*Ra*T_i)*dx
```

```

787 rp = -p_t*div(v_i)*dx
788 rT = (T_t*inner(v_i, grad(T_i)) + inner(grad(T_t), grad(T_i)))*dx
789 r = rv + rp + rT
790 J = derivative(r, u_i, u_a)

```

Listing 4 Weak form of Stokes thermal convection system

791 For the sake of brevity we have assumed that the most recent iterated solutions, \mathbf{v}_i ,
792 \mathbf{p}_i and \mathbf{T}_i , and test functions, \mathbf{v}_t , \mathbf{p}_t and \mathbf{T}_t , have been declared. The individual
793 solutions are part of a larger system solution, $\mathbf{u}_i=(\mathbf{v}_i, \mathbf{p}_i, \mathbf{T}_i)$, and a trial function
794 for the system also exists, $\mathbf{u}_a=(\mathbf{v}_t, \mathbf{p}_t, \mathbf{T}_t)$. Additionally the unit vector in the
795 direction of gravity, `gravity`, the Rayleigh number, `Ra`, and the viscosity, `eta`, have
796 been declared with the latter either being 1 in the isoviscous case or a function of
797 temperature, \mathbf{T}_i , in the temperature-dependent case. In either case the Jacobian
798 matrix, \mathbf{J} , is easily obtained using the `derivative` function. Using this and the residual
799 \mathbf{r} allow (78) to be repeatedly solved for \mathbf{u}_i until convergence is achieved and the
800 root of the residual found.

801 *Picard's method* Convergence of the Newton iteration method depends on having
802 a good initial guess, which is not always possible, especially when solving steady-
803 state problems like (70)–(72). In this case an alternative approach is to use a Picard
804 iteration. This splits the equations into multiple linearized subsets and solves them
805 sequentially and repeatedly, updating the nonlinear terms at each iteration, until
806 convergence is achieved. Equations (70)–(72) can be split into two systems of the
807 form of (8), the first for the Stokes system

$$808 \quad \mathbf{S}_s = \begin{pmatrix} \mathbf{K}_s & \mathbf{G}_s \\ \mathbf{D}_s & \mathbf{0} \end{pmatrix} \quad (79)$$

$$809 \quad \mathbf{K}_s = K_{s_{i_1 j_1}} = \sum_k \int_{e_k} \left(\frac{\nabla \vec{\omega}_{i_1} + \nabla \vec{\omega}_{i_1}^T}{2} \right) : 2\eta \left(\frac{\nabla \vec{\omega}_{j_1} + \nabla \vec{\omega}_{j_1}^T}{2} \right) dx \quad (80)$$

$$810 \quad \mathbf{G}_s = G_{s_{i_1 j_2}} = - \sum_k \int_{e_k} \nabla \cdot \vec{\omega}_{i_1} \chi_{j_2} dx \quad (81)$$

$$811 \quad \mathbf{D}_s = D_{s_{i_2 j_1}} = - \sum_k \int_{e_k} \chi_{i_2} \nabla \cdot \vec{\omega}_{j_1} dx \quad (82)$$

$$812 \quad \mathbf{u}_s = (\mathbf{v}, \mathbf{P})^T = (\vec{v}_{j_1}, P_{j_2})^T \quad (83)$$

$$813 \quad \mathbf{f}_s = f_{s_{i_1}} = - \sum_k \int_{e_k} \vec{\omega}_{i_1} \cdot \hat{g} Ra \tilde{T} dx \quad (84)$$

814

815 and the second for the temperature equation

$$816 \quad \mathbf{S}_T = S_{T_{ij}} = \sum_k \int_{e_k} \left(\phi_i \tilde{v} \cdot \nabla \phi_j + \nabla \phi_i \cdot \nabla \phi_j \right) dx \quad (85)$$

$$817 \quad \mathbf{u}_T = \mathbf{T} = T_j \quad (86)$$

$$818 \quad \mathbf{f}_T = f_{T_i} = 0 \quad (87)$$

819

820 For UFL code snippets of (79) and (84) see listing 5

```

821 Ks = inner(sym(grad(v_t)), 2*eta*sym(grad(v_a)))*dx 1
822 Gs = -div(v_t)*p_a*dx 2
823 Ds = -p_t*div(v_a)*dx 3
824 Ss = Ks + Gs + Ds 4
825 fs = -inner(v_t, gravity)*Ra*T_i*dx 5

```

Listing 5 Weak form of Stokes system

826 and for (85) see listing 6.

```

827 ST = (T_t*inner(v_i, grad(T_a)) + inner(grad(T_t), grad(T_a)))*dx 1

```

Listing 6 Weak form of Stokes thermal convection system

828 The full system solution vector remains $\mathbf{u}=(\mathbf{u}_s, \mathbf{u}_T)^T=(\mathbf{v}, \mathbf{P}, \mathbf{T})^T$ and the best
829 guess at the solution is \mathbf{u}^i . $\mathbf{S}_s(\mathbf{u}^i)\mathbf{u}_s^{i+1}=\mathbf{f}_s(\mathbf{u}_s^i)$ is solved for \mathbf{u}_s^{i+1} , which is used to
830 update \mathbf{u} such that $\mathbf{u}_s^{i+1}\rightarrow\mathbf{u}_s^i$ before solving $\mathbf{S}_T(\mathbf{u}^i)\mathbf{u}_T^{i+1}=\mathbf{0}$ for an updated solution
831 for temperature, \mathbf{u}_T^{i+1} . Repeating this iteration will generally find the root of the
832 residuals (74)–(76) and once again the iteration is repeated until $\mathbf{r}=\mathbf{0}$ in some norm
833 and to some tolerance.

834 If the initial guess is sufficiently good then Newton should converge quadrat-
835 ically while a Picard iteration will converge at a lower rate. However neither con-
836 vergence nor the convergence rate of either method is guaranteed. Various methods
837 are available for solutions that do not converge. These include finding a better ini-
838 tial guess (e.g., a solution from a case with lower convective vigor), “relaxing” the
839 solution by only applying a partial update at each iteration, or linearizing terms in
840 the Jacobian matrix. It should also be noted that, if applied to the linear problems
841 discussed in previous sections, any nonlinear iteration should converge in a single
842 iteration.

843 *Diagnostics* The geometry and expressions for the boundary conditions for the se-
844 lected Blankenbach et al. (1989) cases are shown in Figure 6a and a converged model
845 solution for temperature and velocity obtained for $Ra=10^4$ (benchmark case 1a from
846 Blankenbach et al., 1989) is shown in Figure 6b. To quantify the precision with which
847 the governing equations can be solved we focus on two measures of convective vigor.
848 The first is the Nusselt number Nu which is the integrated nondimensional surface
849 heatflow

$$850 \quad Nu = - \int_0^1 \frac{\partial T}{\partial y}(x, y = 1) dx \quad (88)$$

851 The second is the root-mean-square velocity V_{rms} defined as

$$852 \quad V_{\text{rms}} = \sqrt{\frac{\int_{\Omega} \vec{v} \cdot \vec{v} dx}{\int_{\Omega} dx}} \quad (89)$$

853 Table 9 in Blankenbach et al. (1989) specifies their best estimates for various quan-
854 tities of the benchmark. We will focus on Nu and V_{rms} and show results for their
855 steady-benchmarks 1a–1c (isoviscous, $\eta=1$, with Ra increasing from 10^4 to 10^5 and
856 10^6) and benchmark 2a which has $Ra=10^4$ and a temperature-dependent viscosity
857 $\eta(T)=\exp(-bT)$ with $b=\ln(10^3)$ (see Table 1).

858 *Discretization* For the Stokes equation TerraFERMA uses the P2P1 Taylor-Hood
 859 Lagrange element pair for the shape functions $(\bar{\omega}_j, \chi_j)$ (as in section 2.2.5) and P2
 860 elements for the heat equation (ϕ_j) . The choice of elements here can be tersely de-
 861 scribed as P2P1P2. In TerraFERMA we apply a Newton iteration to cases 1a–c with
 862 a harmonic perturbation to the conductive state $T(x, y) = 1 - y + 0.1 \cos \pi x \sin \pi y$
 863 as an initial guess for temperature and the solution to $\mathbf{S}_s \mathbf{u}_s = \mathbf{f}_s$ given the initial T
 864 as a first guess for velocity and pressure. We use a Picard iteration and an isoviscous
 865 initial velocity and pressure guess for case 2 owing to the difficulty getting Newton
 866 to converge without a better initial guess. Both are solved to a relative tolerance,
 867 ϵ_{rtol} , of 10^{-9} .

868 We also show results obtained with Sepran using the same P2P1P2 discretiza-
 869 tion as in TerraFERMA. The same initial guess is used for case 1a, but for 1b
 870 and 2a we use the final solution from 1a as an initial guess and for 1c we use the
 871 final solution of 1b. Picard iteration is used for all cases to a relative tolerance of
 872 10^{-9} .

873 *Results* We obtain results for grids with 32, 64, 128, and 256 elements on a side.
 874 The TerraFERMA results have grid refinement towards the edges of the domain
 875 to allow for better resolution of the thermal boundary layer at a lower number
 876 of grid points. The Sepran results are obtained on equidistant meshes where the
 877 computation of (88) is improved following the method of Ho-Liu et al. (1987). We
 878 follow Blankenbach et al. (1989) in using Richardson extrapolation to attempt to
 879 find the “best” estimate as shown in comparison to theirs in Table 1. We make
 880 estimates from the modeling approaches independently and average them to find
 881 the “new” results. A brief inspection suggests that the estimates made in 1989 were
 882 clearly rather precise!

883 Figure 7 shows how our model predictions trend toward our average extrapo-
 884 lated values. Note that these are not convergence plots like those used previously
 885 when we compared the approximate solution to the analytical solution. Here, the
 886 best estimates do not represent metrics obtained from an analytical solution. Some
 887 of the flattening or ‘V’-ing in the curves is due to the change in sign of the dif-
 888 ference between the modeled and extrapolated values. In general the difference
 889 between approximate solution and extrapolated value is smaller at lower convective
 890 vigor (compare 1a and 1c) and larger with stronger nonlinearities (compare 1a and
 891 2a).

Table 1 Best values from (Blankenbach et al., 1989) and our averaged extrapolated values from current models for selected benchmark values (see text)

case	Ra	η	Blankenbach et al. (1989)		updated estimates	
			Nu	V_{rms}	Nu	V_{rms}
1a	10^4	1	4.884409	42.864947	4.88440907	42.8649484
1b	10^5	1	10.534095	193.21454	10.53404	193.21445
1c	10^6	1	21.972465	833.98977	21.97242	833.9897
2a	10^4	$e^{-\ln(10^3)T}$	10.0660	480.4334	10.06597	480.4308

892 2.3 FEM determination of SZ thermal structure

893 2.3.1 Recap of the governing equations

894 While we already encountered examples of solution of the governing equations (12)–
 895 (14), we will formulate the full set of equations for subduction zone thermal structure

below for clarity and completeness' sake. We will set up the parameters and equations in a general form that we will use in part III for a global suite of models (similar to those in Syracuse et al. (2010) and Wada and Wang (2009)) but restrict ourselves in this part to applying them to a simplified benchmark problem. The equations will be introduced in dimensional form before nondimensionalizing them in section 2.3.2. All dimensional variables will be indicated by a superscript *. Dimensional reference values will be indicated by the subscript ₀. We assume a 2D Cartesian coordinate system with coordinates $\vec{x}^* = (x_1^*, x_2^*)^T = (x^*, y^*)^T = (x^*, -z^*)^T$ where z^* is depth.

Conservation of mass under the assumption that the fluid is incompressible leads to

$$\nabla^* \cdot \vec{v}^* = 0 \quad (90)$$

where, in two-dimensions, $\vec{v}^* = (v_1^*, v_2^*)^T = (v_x^*, v_y^*)^T$ is the velocity vector. Assuming all flow is driven by a kinematic boundary condition, conservation of momentum leads to the dimensional Stokes equation without buoyancy forces

$$-\nabla^* \cdot \boldsymbol{\tau}^* + \nabla^* P^* = 0 \quad (91)$$

where P^* is the dynamic pressure and $\boldsymbol{\tau}^*$ is the deviatoric stress tensor given by

$$\boldsymbol{\tau}^* = 2\eta^* \dot{\boldsymbol{\epsilon}}^* \quad (92)$$

Here, η^* is dynamic viscosity and $\dot{\boldsymbol{\epsilon}}^*$ is the deviatoric strain-rate tensor with components

$$\dot{\epsilon}_{ij}^* = \frac{1}{2} \left[\frac{\partial v_i^*}{\partial x_j^*} + \frac{\partial v_j^*}{\partial x_i^*} \right] \quad (93)$$

The time-dependent dimensional heat equation is given by

$$\rho^* c_{p0} \left(\frac{\partial T^*}{\partial t^*} + \vec{v}^* \cdot \nabla^* T^* \right) = \nabla^* \cdot (k^* \nabla^* T^*) + H^* \quad (94)$$

while, in cases where a steady state is assumed ($\frac{\partial T^*}{\partial t^*} = 0$) temperature is governed by

$$\rho^* c_{p0} \vec{v}^* \cdot \nabla^* T^* = \nabla^* \cdot (k^* \nabla^* T^*) + H^* \quad (95)$$

where ρ^* is density, c_{p0} is the heat capacity at constant pressure (assumed constant), T^* is temperature, k^* is thermal conductivity, and H^* is volumetric heat production. In this paper we will assume that the viscosity η^* is either constant, $\eta^* = \eta_0$, or is a function of temperature and strain rate following a simplified creep law for dislocation creep in dry olivine from Karato and Wu (1993)

$$\eta_{\text{disl}}^* = A_\eta^* \exp \left(\frac{E^*}{nR^*(T^* + T_a^*)} \right) \dot{\epsilon}_{II}^{*\frac{1-n}{n}} \quad (96)$$

928 where A_η^* is a prefactor, E^* is the activation energy, R^* is the gas constant, n is
 929 a powerlaw index, T_a^* a linear approximation of an adiabatic temperature using a
 930 gradient of $0.3^\circ\text{C}/\text{km}$ with $T_a^*=0$ at the top of the model (which may not be at
 931 $z^*=0$ due to assumptions of ocean bathymetry as we will see in section 2.3.3) and
 932 $\dot{\epsilon}_{II}^*$ is the second invariant of the deviatoric strain-rate tensor (also known as the
 933 effective deviatoric strain rate)

$$934 \quad \dot{\epsilon}_{II}^* = \sqrt{\frac{1}{2} \dot{\epsilon}^* : \dot{\epsilon}^*} \quad (97)$$

935 Since the dynamical range of the viscosity (96) is large over the temperature contrast
 936 across subduction zones it is common practice to cap the viscosity at some arbitrary
 937 maximum η_{\max}^* so that in the variable viscosity case

$$938 \quad \eta^* = \left(\frac{1}{\eta_{\text{disl}}^*} + \frac{1}{\eta_{\max}^*} \right)^{-1} \quad (98)$$

939 **Table 2** Nomenclature and reference values

Quantity	Symbol	Nominal value	Nondimensional value
Reference temperature scale	T_0	1 K=1°C	-
Surface temperature	T_s^*	273 K=0°C	$T_s=0$
Mantle temperature	T_m^*	1623 K=1350°C	$T_m=1350$
Surface heat flow ^c	q_s^*	§W/m ²	q_s^* §
Reference density	ρ_0	3300 kg/m ³	-
Crustal density ^c	ρ_c^*	2750 kg/m ³	$\rho_c=0.833333$
Mantle density	ρ_m^*	3300 kg/m ³	$\rho_m=1$
Reference thermal conductivity	k_0	3.1 W/(m K)	-
Crustal thermal conductivity ^c	k_c^*	2.5 W/(m K)	$k_c=0.8064516$
Mantle thermal conductivity	k_m^*	3.1 W/(m K)	$k_m=1$
Volumetric heat production (upper crust) ^c	H_1^*	1.3 μW/m ³	$H_1=0.419354$
Volumetric heat production (lower crust) ^c	H_2^*	0.27 μW/m ³	$H_2=0.087097$
Age of overriding crust ^o	A_c^*	§Myr	A_c^* §
Age of subduction ^t	A_s^*	§Myr	A_s^* §
Age of subducting slab	A^*	§Myr	A^* §
Reference length scale	h_0	1 km	-
Depth of base of upper crust ^c	z_1^*	15 km	$z_1=15$
Depth of base of lower crust (Moho)	z_2^*	§km	z_2^* §
Trench depth	z_{trench}^*	§km	z_{trench}^* §
Position of the coast line	x_{coast}^*	§km	x_{coast}^* §
Wedge inflow/outflow transition depth	z_{io}^*	§km	z_{io}^* §
Depth of domain	D^*	§km	D^* §
Width of domain	L^*	§km	L^* §
Depth of change from decoupling to coupling	d_c^*	80 km	$d_c=80$
Reference heat capacity	c_{p0}	1250 J/(kg K)	-
Reference thermal diffusivity	κ_0	$0.7515 \times 10^{-6} \text{ m}^2/\text{s}$	-
Activation energy	E	540 kJ/mol	-
Powerlaw exponent	n	3.5	-
Pre-exponential constant	A_η^*	$28968.6 \text{ Pa s}^{1/n}$	-
Reference viscosity scale	η_0	10^{21} Pa s	-
Viscosity cap	η_{\max}^*	10^{25} Pa s	-
Gas constant	R^*	8.3145 J/(mol K)	-
Derived velocity scale	v_0	23.716014 mm/yr	-
Convergence velocity	V_s^*	§mm/yr	V_s^* §

^c ocean-continent subduction only

^o ocean-ocean subduction only

^t time-dependent simulations only

§ varies between models

940 *2.3.2 Nondimensionalization*

941 It is attractive to nondimensionalize the equations such that most quantities are
 942 scaled to be close to 1. This provides simple scaling arguments to allow for under-
 943 standing which terms in the equations are dominant, avoids computer algebra that
 944 mixes very large and very small numbers, and provides for the formation of a matrix-
 945 vector system where the condition number of the matrix (Golub and Van Loan,
 946 1989) is more optimal.

947 Table 2 provides a list of dimensional reference values, dimensional parame-
 948 ters, and their nondimensional equivalents. For the nondimensionalization of (90)–
 949 (98) we use the diffusional time scaling with nondimensional time defined as
 950 $t=t^*\kappa_0/h_0^2$ where h_0 is the reference length scale and κ_0 is the reference ther-
 951 mal diffusivity. With $\vec{x}=\vec{x}^*/h_0$ it follows $\vec{v}=\vec{v}^*h_0/\kappa_0$, $\dot{\epsilon}=\dot{\epsilon}^*h_0^2/\kappa_0$, and $\nabla=\nabla^*h_0$.
 952 We further introduce $T=(T^* - T_s^*)/T_0$, $k=k^*/k_0$, $\rho=\rho^*/\rho_0$, $P=P^*h_0^2/(\kappa_0\eta_0)$, and
 953 $H=H^*h_0^2/(\rho_0c_{p0}T_0\kappa_0)$. Note that our choices of T_0 and h_0 in Table 2 cause the
 954 numerical values of dimensional position (in km) and temperature (in °C) to have
 955 the same magnitude as the corresponding nondimensional quantities. Substitution
 956 of the nondimensional variables and constants leads to the following set of nondi-
 957 mensional equations for pressure and velocity

958
$$\nabla \cdot \vec{v} = 0 \tag{99}$$

959
 960
$$-\nabla \cdot \left(2\eta \frac{\nabla \vec{v} + \nabla \vec{v}^T}{2} \right) + \nabla P = 0 \tag{100}$$

961 and either a time-dependent equation for temperature

962
$$\rho \left(\frac{\partial T}{\partial t} + \vec{v} \cdot \nabla T \right) = \nabla \cdot (k \nabla T) + H \tag{101}$$

963 or its equivalent when a steady-state solution is assumed

964
$$\rho \vec{v} \cdot \nabla T = \nabla \cdot (k \nabla T) + H \tag{102}$$

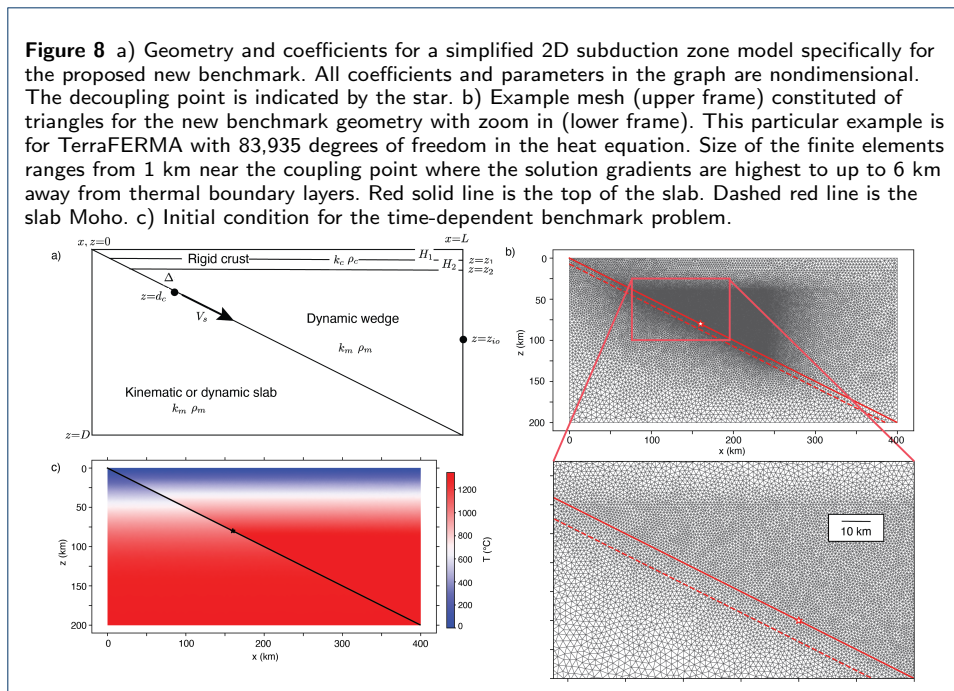
965 The viscosity η is either constant 1 or follows from the dislocation creep formulation
 966 (96) with cap (98) as

967
$$\eta = \frac{\eta^*}{\eta_0} \tag{103}$$

968 Note that for simplicity as well as clarity we form the viscosity function (98) in
 969 dimensional form and nondimensionalize the viscosity with the reference viscosity
 970 η_0 .

971 *2.3.3 Geometry, boundary conditions, and initial conditions*

972 A simplified version of the typical geometry used in 2D subduction zone modeling
 973 with a kinematically prescribed slab is shown in Figure 8a. The model is a 2D
 974 Cartesian box of width L and depth D . We picture a model with a straight slab
 975 surface here but it can also be constructed from a natural spline through a set



976 of control points as in Syracuse et al. (2010) or connected linear segments with
 977 different angles with respect to the horizontal as in Wada and Wang (2009). In
 978 the models following the geometries of Syracuse et al. (2010) described in part III
 979 this simplified geometry is modified by including a curved slab and a coastline. At
 980 $x=0$ the top of the model is at $(0, z_{\text{trench}})^T$, for a given depth of the trench, z_{trench} .
 981 Between $x=0$ and $x=x_{\text{coast}}$, the presumed horizontal position of the coast, the top
 982 of the model shallows linearly to $(x_{\text{coast}}, 0)^T$. For $x > x_{\text{coast}}$ the top of the model
 983 is at $z=0$. Actual choices for these parameters are provided in the Supplementary
 984 Information. The kinematic slab approach requires at a minimum that the slab
 985 surface velocity with magnitude V_s is prescribed. The velocity in the slab, \vec{v}_s , can
 986 be determined from the solution of (99)–(100) in the slab (resulting in an extra
 987 Stokes equation owing to the discontinuity in velocity and pressure required across
 988 the slab above the coupling depth). Alternatively, the velocity in the slab can also
 989 be simply prescribed by defining the internal slab velocity to be parallel to and of
 990 same magnitude as that of the point on the slab surface closest to the point internal
 991 to the slab. For a straight-dipping slab we have found that either approach leads
 992 to very similar temperature solutions; for a curved slab the use of temperature-
 993 dependent viscosity also yields very similar temperature solution at the top of the
 994 slab for these two approaches. Here, we take the approach of solving for the velocity
 995 in the slab, solving (101) for temperature T in the whole domain and two Stokes
 996 equations (99)–(100), one in the wedge for \vec{v} and P and one in the slab for $\vec{v}=\vec{v}_s$
 997 and $P=P_s$. The velocity in the overriding plate, above the slab and down to $z=z_2$,
 998 is always prescribed as $\vec{v}=0$ and the Stokes equation is not solved here.

999 We use an unstructured mesh of triangular elements to discretize the domain. A
 1000 typical example, with 1 km element resolution in the region with the most activity is
 1001 shown in Figure 8b. On this mesh we define discrete approximate discrete solutions

1002 for velocity, pressure and temperature as

$$1003 \quad \vec{v} \approx \tilde{\vec{v}} = \sum_j \omega_j^k v_j^k \quad (104)$$

$$1004 \quad P \approx \tilde{P} = \sum_j \chi_j P_j \quad (105)$$

$$1005 \quad T \approx \tilde{T} = \sum_j \phi_j T_j \quad (106)$$

1007 with similarly defined discrete test functions, \tilde{v}_t , \tilde{P}_t and \tilde{T}_t using the same shape
 1008 functions $\vec{\omega}_j = \omega_j^k$, χ_j and ϕ_j for velocity, pressure and temperature at each DOF
 1009 j respectively. In the results presented using TerraFERMA we use a P2P1P2 dis-
 1010 cretization where $\vec{\omega}_j$ are piecewise-quadratic, χ_j are piecewise linear and ϕ_j are
 1011 piecewise-quadratic continuous Lagrange functions. The results from Sepran use
 1012 either the same P2P1P2 discretization (indicated by TH) or a penalty function
 1013 method (indicated by PF) with quadratic P2 Crouzeix-Raviart (rather than La-
 1014 grange) shape functions for the velocity ($\vec{\omega}_j$). In this method the dynamic pressure
 1015 is eliminated from the Stokes equation (70) by a perturbation of the incompress-
 1016 ibility constraint, that is, $\nabla \cdot \vec{v} = \epsilon_P P$ where ϵ_P is a small number. We use $\epsilon_P = 10^{-6}$
 1017 here; see Cuvelier et al. (1986) or King et al. (1990) for details on the elimination
 1018 process. This method leads to a smaller stiffness matrix compared to that when
 1019 using Taylor-Hood elements since the pressure unknowns are eliminated. It also
 1020 results in a positive definite matrix for which more efficient direct solution methods
 1021 exist. For the temperature shape functions (ϕ_j) Sepran also uses quadratic Lagrange
 1022 polynomials (resulting in a combined P2P2 discretization). In the penalty function
 1023 approach pressure is eliminated from the equations so χ_j are not used.

1024 For the heat equation (101) we assume homogeneous natural (or Neumann)
 1025 boundary conditions along the geometry where the velocity vector points out of
 1026 the box (i.e., an outflow boundary). At the trench inflow boundary we assume a
 1027 half-space cooling model $T_{\text{trench}}(z)$ given by

$$1028 \quad \tilde{T}(x=0, z) = T_{\text{trench}}(z) = T_s + (T_m - T_s) \operatorname{erf} \left(\frac{z - z_{\text{trench}}}{z_d} \right) \quad (107)$$

1029 where T_s is the nondimensional surface temperature, T_m the nondimensional mantle
 1030 temperature, z_{trench} is the nondimensional depth of the trench, and the nondimen-
 1031 sional scale depth z_d is proportional to the dimensional age of the incoming litho-
 1032 sphere A^* via $z_d = 2 \frac{\sqrt{\kappa_0 A^*}}{h_0}$.

1033 Details of the backarc temperature depend on whether we are modeling ocean-
 1034 continent or ocean-ocean subduction. In the ocean-continent case we assume a con-
 1035 stant surface heat flow q_s and radiogenic heat production H . We use a two-layer
 1036 crustal model with density $\rho = \rho_c$, thermal conductivity $k = k_c$ and heat production
 1037 $H = H_1$ from depth 0 to z_1 and heat production $H = H_2$ between depths z_1 and z_2 ,
 1038 where z_1 and z_2 vary between subduction zones. The mantle portion of the model
 1039 (in both the slab and the wedge) is assumed to have density $\rho = \rho_m$, conductivity
 1040 $k = k_m$, and zero heat production $H = 0$. At the backarc the wedge inflow boundary
 1041 condition on temperature is chosen to be a geotherm $T_{\text{backarc}}(z)$ consistent with

1042 these parameters, that is

$$1043 \quad \tilde{T}(x = L, z) = T_{\text{backarc},c}(z) = \begin{cases} T_s - \frac{H_1 z^2}{2k_c} + \frac{q_s}{k_c} z & : 0 \leq z \leq z_1 \\ T_{\text{backarc},c}(z = z_1) - \frac{H_2(z-z_1)^2}{2k_c} + \frac{q_1}{k_c}(z - z_1) & : z_1 < z \leq z_2 \\ \min(T_m, T_{\text{backarc},c}(z = z_2) + \frac{q_2}{k_m}(z - z_2)) & : z_2 < z \leq z_{i_o} \end{cases} \quad (108)$$

1044 The discrete heat flow values q_i are the heat flow at the crustal boundaries at depth
 1045 $z=z_i$ that can be found as $q_1=q_s-H_1z_1$ and $q_2=q_1-H_2(z_2-z_1)$. In the ocean-ocean
 1046 case we use a one-layer crustal model (z_1 is not defined), heat production is zero
 1047 ($H=0$) and the density and thermal conductivity are set to respectively $\rho=\rho_m$ and
 1048 $k=k_m$ everywhere. The wedge inflow boundary condition on temperature down to
 1049 z_{i_o} is then

$$1050 \quad \tilde{T}(x = L, z) = T_{\text{backarc},o}(z) = T_s + (T_m - T_s)\text{erf}\left(\frac{z}{z_c}\right) \quad (109)$$

1051 where z_c is related to the dimensional age of the overriding plate A_c^* minus the age
 1052 of subduction A_s^* via $z_c = 2\sqrt{\frac{\kappa_0(A_c^* - A_s^*)}{h_0}}$. Below z_{i_o} we assume again a homogeneous
 1053 Neumann boundary condition for temperature.

1054 For the two Stokes equations we assume homogeneous (zero stress) Neumann
 1055 boundary condition on \tilde{v} and \tilde{P} for the wedge in and outflow and on \tilde{v}_s and \tilde{P}_s
 1056 for the slab in and outflow. The top of the wedge at $z=z_2$ is a rigid boundary, $\tilde{v}=0$,
 1057 consistent with the imposition of zero flow in the overriding plate. The wedge flow,
 1058 \tilde{v} , is driven by the coupling of the slab to the wedge below a coupling depth. This
 1059 is implemented by a Dirichlet boundary condition along the slab surface. Above
 1060 the coupling depth we impose zero velocity. Below the coupling depth the velocity
 1061 is parallel to the slab and has magnitude V_s . It has been found that a smooth
 1062 transition from zero to full speed over a short depth interval enhances the accuracy
 1063 of the Stokes solution (see discussion in van Keken et al. (2002) and equations
 1064 (13)–(15) in van Keken et al. (2008)) so here coupling begins at $z=d_c$ and ramps up
 1065 linearly until full coupling is reached at $z=d_c+2.5$. For improved numerical accuracy
 1066 we specify nodal points at these depths in all models presented here and in part III.
 1067 At the top of the wedge we imposed a rigid Dirichlet boundary condition at the
 1068 base of the Moho on the wedge velocity, $\tilde{v}=0$. The slab flow, \tilde{v}_s , is driven by the
 1069 imposition of a Dirichlet boundary condition parallel to the slab with magnitude
 1070 V_s along the entire length of the slab surface, resulting in a discontinuity between
 1071 \tilde{v} and \tilde{v}_s above $z=d_c+2.5$.

1072 In the case of time-dependent simulations we require an initial condition T^0 .
 1073 We use an initial condition where the temperature on the slab side is given by
 1074 T_{trench} (107). Above the slab we use $T_{\text{backarc},c}$ (108) for ocean-continent subduction
 1075 or $T_{\text{backarc},o}$ (109) for ocean-ocean subduction. Figure 8c shows the initial condition
 1076 used in the time-dependent benchmark comparison below.

1077 2.3.4 Solution strategy

1078 Sections 2.3.2–2.3.3 describe a set of nonlinear, potentially time-dependent equa-
 1079 tions and boundary conditions for the temperature, velocity, and dynamic pressure

1080 in a subduction zone. To find their solution we wish to find the root of the residual
 1081 $\mathbf{r} = \mathbf{r}_{\tilde{v}} + \mathbf{r}_P + \mathbf{r}_{\tilde{v}_s} + \mathbf{r}_{P_s} + \mathbf{r}_T$, where

$$1082 \quad \mathbf{r}_{\tilde{v}} = r_{\tilde{v}_{i_1}} := \int_{\Omega_{\text{wedge}}} \left[\left(\frac{\nabla \tilde{\omega}_{i_1} + \nabla \tilde{\omega}_{i_1}^T}{2} \right) : 2\eta \left(\frac{\nabla \tilde{v} + \nabla \tilde{v}^T}{2} \right) - \nabla \cdot \tilde{\omega}_{i_1} \tilde{P} \right] dx = 0 \quad (110)$$

$$1083 \quad \mathbf{r}_P = r_{P_{i_2}} := - \int_{\Omega_{\text{wedge}}} \chi_{i_2} \nabla \cdot \tilde{v} dx = 0 \quad (111)$$

$$1084 \quad \mathbf{r}_{\tilde{v}_s} = r_{\tilde{v}_{s i_3}} := \int_{\Omega_{\text{slab}}} \left[\left(\frac{\nabla \tilde{\omega}_{i_3} + \nabla \tilde{\omega}_{i_3}^T}{2} \right) : 2\eta \left(\frac{\nabla \tilde{v}_s + \nabla \tilde{v}_s^T}{2} \right) - \nabla \cdot \tilde{\omega}_{i_3} \tilde{P}_s \right] dx = 0 \quad (112)$$

$$1085 \quad \mathbf{r}_{P_s} = r_{P_{s i_4}} := - \int_{\Omega_{\text{slab}}} \chi_{i_4} \nabla \cdot \tilde{v}_s dx = 0 \quad (113)$$

1087 and, in the time-dependent case

$$1088 \quad \mathbf{r}_T = r_{T_{i_5}} := \int_{\Omega_{\text{wedge}}} \left[\phi_{i_5} \rho \frac{\partial \tilde{T}}{\partial t} + \phi_{i_5} \tilde{v} \cdot \nabla \tilde{T} + \nabla \phi_{i_5} \cdot k \nabla \tilde{T} \right] dx$$

$$1089 \quad + \int_{\Omega_{\text{slab}}} \left[\phi_{i_5} \rho \frac{\partial \tilde{T}}{\partial t} + \phi_{i_5} \tilde{v}_s \cdot \nabla \tilde{T} + \nabla \phi_{i_5} \cdot k \nabla \tilde{T} \right] dx$$

$$1090 \quad + \int_{\Omega_{\text{crust}}} \left[\phi_{i_5} \rho \frac{\partial \tilde{T}}{\partial t} + \nabla \phi_{i_5} \cdot k \nabla \tilde{T} - \phi_{i_5} H \right] dx = 0 \quad (114)$$

1092 Here, Ω_{wedge} , Ω_{slab} and Ω_{crust} are subsets of the domain corresponding to the
 1093 mantle wedge, slab and overriding crust respectively. We have yet to discretize the
 1094 time derivative $\frac{\partial \tilde{T}}{\partial t}$ in (114). Here we choose to do this using finite differences,
 1095 approximating the derivative by the difference between two discrete time levels

$$1096 \quad \frac{\partial \tilde{T}}{\partial t} \approx \frac{\tilde{T}^{n+1} - \tilde{T}^n}{\Delta t^n} \quad (115)$$

1097 where $\Delta t^n = t^{n+1} - t^n$ is the time-step, the difference between the old and new
 1098 times, and \tilde{T}^{n+1} and \tilde{T}^n represent the solution at these time levels. It then only
 1099 remains to define at what time level the other coefficients in (114) are evaluated
 1100 and we do this using a “theta”- scheme such that

$$1101 \quad \mathbf{r}_T = r_{T_{i_5}} := \int_{\Omega_{\text{wedge}}} \left[\phi_{i_5} \rho \left(\frac{\tilde{T}^{n+1} - \tilde{T}^n}{\Delta t^n} \right) + \phi_{i_5} \tilde{v}^\theta \cdot \nabla \tilde{T}^\theta + \nabla \phi_{i_5} \cdot k \nabla \tilde{T}^\theta \right] dx$$

$$1102 \quad + \int_{\Omega_{\text{slab}}} \left[\phi_{i_5} \rho \left(\frac{\tilde{T}^{n+1} - \tilde{T}^n}{\Delta t^n} \right) + \phi_{i_5} \tilde{v}_s^\theta \cdot \nabla \tilde{T}^\theta + \nabla \phi_{i_5} \cdot k \nabla \tilde{T}^\theta \right] dx$$

$$1103 \quad + \int_{\Omega_{\text{crust}}} \left[\phi_{i_5} \rho \left(\frac{\tilde{T}^{n+1} - \tilde{T}^n}{\Delta t^n} \right) + \nabla \phi_{i_5} \cdot k \nabla \tilde{T}^\theta - \phi_{i_5} H \right] dx = 0 \quad (116)$$

1105 where $\tilde{v}^\theta = \theta_v \tilde{v}^{n+1} + (1 - \theta_v) \tilde{v}^n$, $\tilde{v}_s^\theta = \theta_v \tilde{v}_s^{n+1} + (1 - \theta_v) \tilde{v}_s^n$, and $\tilde{T}^\theta = \theta \tilde{T}^{n+1} + (1 -$
 1106 $\theta) \tilde{T}^n$, and $\theta_v, \theta \in [0, 1]$ are parameters controlling what time level the coefficients
 1107 are evaluated at. The parameter θ controls the stability and accuracy of the time-
 1108 integration scheme. Common choices are $\theta=0$ (explicit Euler), $\theta=1$ (implicit Euler),
 1109 and $\theta=0.5$ (Crank-Nicolson).

1110 At each time level (110)–(113) and (116) represent a nonlinear problem, which
 1111 we solve using a Picard iteration, first solving (116) then solving (110)–(113)
 1112 using the most up to date temperature, \tilde{T}^{n+1} , and repeating until the root of
 1113 the residual, \mathbf{r} , is found to some tolerance. The time level and all solution vari-
 1114 ables are then updated and a new time level and new Picard iteration com-
 1115 menced. The time-step Δt^n is chosen such that the maximum Courant number,
 1116 $c_{\max}^n = \max \left(\frac{\max(\tilde{v}^n) \Delta t^n}{h_e}, \frac{\max(\tilde{v}_s^n) \Delta t^n}{h_e} \right)$, where h_e is a measure of the local element
 1117 size, does not exceed some critical value, $c_{\max}^n \leq c_{\text{crit}}$. This procedure is repeated
 1118 until the final time (the age of subduction, A_s^*) is reached.

1119 If we are seeking the steady-state solution ($\frac{\partial T}{\partial t} = 0$), we solve (110)–(113) but
 1120 (114) becomes

$$\begin{aligned}
 1121 \quad \mathbf{r}_T = r_{T_{i_5}} &:= \int_{\Omega_{\text{wedge}}} \left[\phi_{i_5} \tilde{v} \cdot \nabla \tilde{T} + \nabla \phi_{i_5} \cdot k \nabla \tilde{T} \right] dx \\
 1122 &+ \int_{\Omega_{\text{slab}}} \left[\phi_{i_5} \tilde{v}_s \cdot \nabla \tilde{T} + \nabla \phi_{i_5} \cdot k \nabla \tilde{T} \right] dx \\
 1123 &+ \int_{\Omega_{\text{crust}}} \left[\nabla \phi_{i_5} \cdot k \nabla \tilde{T} - \phi_{i_5} H \right] dx = 0 \quad (117) \\
 1124
 \end{aligned}$$

1125 where a theta-scheme approach is no longer required because no time levels exist.
 1126 A Picard iteration is used to approximately find $\mathbf{r} = \mathbf{0}$, this time solving (110)–(113)
 1127 first followed by (117). At the beginning of the simulation we find an isoviscous
 1128 ($\eta=1$) solution to (110)–(113) to initialize the velocity and pressure.

1129 2.3.5 An optimized subduction zone benchmark

1130 The community subduction zone benchmark in van Keken et al. (2008) provides a
 1131 set of simplified models well suited to test the accuracy of the solution of the gov-
 1132 erning equations that are relevant for subduction zones. Unfortunately, the model
 1133 geometry and assumptions that were chosen at the time are such that they intro-
 1134 duce a few artifacts that do not occur, as best as we know, in any subduction zone
 1135 on Earth. These artifacts include a slab that dips at a constant angle of 45° to
 1136 600 km depth, an overriding plate that excludes continental heat production, and
 1137 imposes slab-wedge coupling at 50 km rather than at 75–80 km depth. The lack of
 1138 crustal heating and the large width of the model, combined with the assumption
 1139 of steady state, lead in the cases with temperature-dependent rheology to a very
 1140 thick top boundary layer. This is caused by the cooling in the lithosphere, which
 1141 results in a gradual thickening of the overriding lid in regions of the model that are
 1142 far away from the arc-side boundary condition. While this is less of a problem in
 1143 time-dependent problems (where time may not be sufficient for significant growth
 1144 of the boundary layer), it shows up dramatically as a “viscous belly” in steady-state
 1145 cases when the model domain is large (as it was in van Keken et al., 2008). In time-
 1146 dependent models it can show up if integration time is very long compared to the

1147 typical age of subduction zones (Hall, 2012). The models in Syracuse et al. (2010)
 1148 avoided this issue by using time integration to only ~ 20 – 40 Myr. The models in
 1149 Wada and Wang (2009) avoided it using steady-state models in a domain that is
 1150 both narrower and shallower than that of the van Keken et al. (2008) benchmark.

1151 To mitigate the artifacts of the previous benchmark we propose a new bench-
 1152 mark model. Modifications include a more shallowly dipping slab that only extends
 1153 to a depth of 200 km, the incorporation of radiogenic heating in the overriding crust
 1154 and a deeper slab-wedge coupling point. We will also replace some of the requested
 1155 model outputs from van Keken et al. (2008) with proper integrals. We will use the
 1156 simplified geometry as in Figure 8 with constant slab dip $\Delta = \tan^{-1}(1/2) = 26.56505^\circ$
 1157 with respect to the horizontal. The maximum depth $D=200$ defines $L=400$. Crustal
 1158 depths z_1 and z_2 are chosen as 15 and 40 respectively. z_{io} depends on wedge ge-
 1159 ometry and rheology and is therefore variable between models. To find this we
 1160 performed a simple iteration in the modeling by setting z_{io} first to a constant value,
 1161 finding the solution to the nonlinear system, determining the actual value of z_{io}
 1162 from the wedge flow, and then imposing this value in a subsequent solution of the
 1163 nonlinear system. While this approach guarantees appropriate implementation of
 1164 the switch from Dirichlet to Neumann boundary condition for the heat equation
 1165 as stated above, we have found that as long as z_{io} is larger than the depth where
 1166 the actual switch between inflow and outflow occurs nearly identical solutions are
 1167 obtained.

1168 We will assume the reference values in Table 2 with case-specific parameters
 1169 given in Table 3. The benchmark assumes ocean-continent subduction with heat
 1170 production in a two-layer crust with crustal density and thermal conductivity (ρ_c
 1171 and k_c respectively) distinct from the mantle (ρ_m and k_m) and a backarc boundary
 1172 condition on temperature given by $T_{\text{backarc},c}(z)$ (108). We will solve (110)–(113)
 1173 either with constant viscosity ($\eta=1$, case 1) or with temperature- and strain-rate-
 1174 dependent viscosity following (103) (case 2). The heat equation will be solved un-
 1175 der the assumption of steady state (117) for the benchmark, but we will also dis-
 1176 cuss some time-dependent results below. For the incoming lithosphere we will as-
 1177 sume $z_d = 97.397$ (corresponding to a dimensional age of the incoming lithosphere
 1178 $A^*=100$ Myr) and convergence speed $V_s=4.2166$ (corresponding to a dimensional
 1179 speed of 10 cm/yr).

1180 **Table 3** Benchmark parameter values.

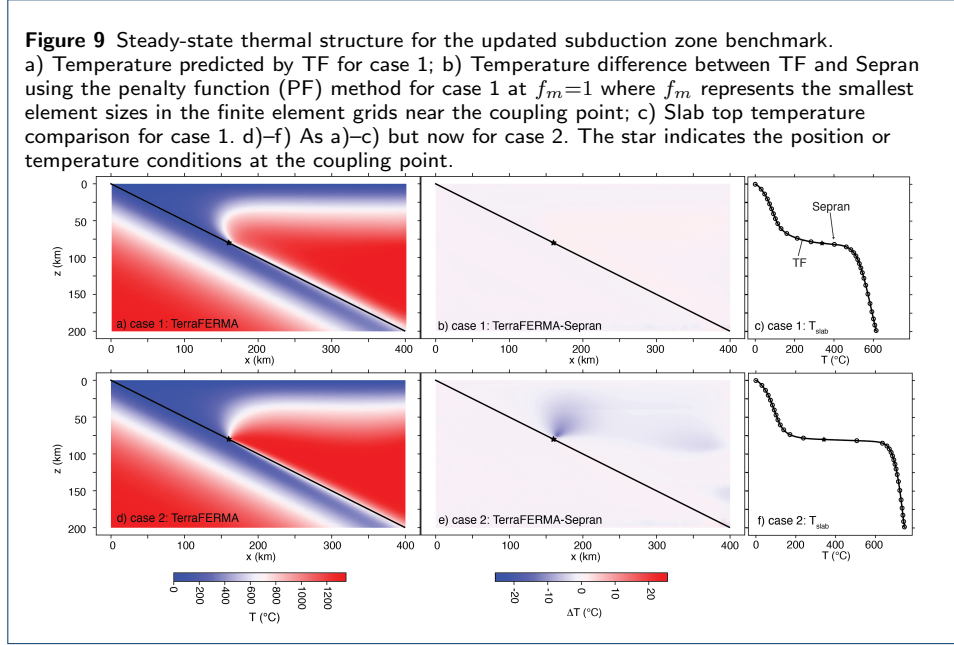
case	type	η	q_s^* (W/m ²)	q_s	A^* (Myr)	z_2	z_{io}	z_{trench}	x_{coast}	D	L	V_s
1	c	1	0.065	20.96774	100	40	139	0	0	200	400	4.2166
2	c	η^*/η_0	0.065	20.96774	100	40	154	0	0	200	400	4.2166

c: ocean-continent subduction

1181 2.3.6 Benchmark comparison TerraFERMA - Sepran

1182 In the benchmark comparison we focus on dimensional metrics representing the
 1183 averaged thermal and velocity structures near the coupling point where gradients
 1184 in velocity and temperature are high. The first metric is the slab temperature at
 1185 100 km depth, $T_{(200,-100)}^*$

$$1186 \quad T_{(200,-100)}^* = T_0 \tilde{T}(x = 200, y = -100) \quad (118)$$



1187 The second metric is the average integrated temperature \bar{T}_s^* along the slab surface
 1188 between depths $z_{s,1}=70$ and $z_{s,2}=120$, that is

$$1189 \quad \bar{T}_s^* = T_0 \frac{\int_{s_1}^{s_2} \tilde{T} ds}{\int_{s_1}^{s_2} ds} \quad (119)$$

1190 where s is distance along the slab top from the trench and $s_1 = \sqrt{5z_{s,1}^2} = 156.5248$
 1191 and $s_2 = \sqrt{5z_{s,2}^2} = 268.32816$. The third metric is the volume-averaged temperature
 1192 \bar{T}_w^* in the mantle wedge corner below the Moho, $z=z_2$ and above where the slab
 1193 surface, $z=z_{\text{slab}}(x)$, is between $z_{s,1}$ and $z_{s,2}$ as defined above

$$1194 \quad \bar{T}_w^* = T_0 \frac{\int_{x=140}^{x=240} \int_{z=z_2}^{z=z_{\text{slab}}(x)} \tilde{T} dz dx}{\int_{x=140}^{x=240} \int_{z=z_2}^{z=z_{\text{slab}}(x)} dz dx} \quad (120)$$

1195 where $z_{\text{slab}}(x) = x/2$. The final metric is the root-mean-squared averaged velocity
 1196 $V_{\text{rms},w}^*$ in the same volume as the third metric, that is

$$1197 \quad V_{\text{rms},w}^* = v_0 \sqrt{\frac{\int_{x=140}^{x=240} \int_{z=z_2}^{z=z_{\text{slab}}(x)} (\tilde{\mathbf{v}} \cdot \tilde{\mathbf{v}}) dz dx}{\int_{x=140}^{x=240} \int_{z=z_2}^{z=z_{\text{slab}}(x)} dz dx}}. \quad (121)$$

1198 Figure 9 shows the temperature fields obtained with TerraFERMA and temperature
 1199 differences between the TerraFERMA and Sepran models. Convergence behavior on
 1200 a series of finer meshes as a function of the number of degrees of freedom in the
 1201 heat equation using the metrics (118)–(121) are shown in Tables 4 and 5.

1202 Note that even on the coarser grids the metrics are generally within less than
 1203 1% from those at the finest grids. The TerraFERMA and Sepran results tend to

1204 converge towards the same limit to reasonable precision for case 1. There seems
 1205 to be a slight, but systematic difference particularly for \bar{T}_w^* and $V_{\text{rms},w}^*$ for case 2.
 1206 Inspection of Figure 9e shows the likely reason for the differences – a systematic
 1207 bubble shows in ΔT right above the coupling point. We attribute this to how the
 two methods treat pressure and we will see more examples of this in part III.

Table 4 Convergence of various metrics describing the solution to the new subduction zone benchmark as a function of degrees of freedom in the heat equation T_{ndof} . The employed meshes have grid refinement in the wedge above and near the coupling point. The factor f_m is representative of the element size near the coupling point. TH=Taylor-Hood; PF=penalty function method. P2P1P2 indicates a discretization that has quadratic shape functions (P2) for velocity and temperature and linear shape functions for pressure (P1). P2P2 is for velocity and temperature only because pressure is eliminated from the Stokes equation in the penalty function method (Cuvelier et al., 1986). In this case $z_{\text{io}}=139$.

f_m	T_{ndof}	$T_{(200,-100)}^*$ (°C)	\bar{T}_s^* (°C)	\bar{T}_w^* (°C)	$V_{\text{rms},w}^*$ (mm/yr)
TerraFERMA TH P2P1P2					
2.0	21403	517.17	451.83	926.62	34.64
1.0	83935	516.95	451.71	926.33	34.64
0.5	332307	516.86	451.63	926.15	34.64
Sepran TH P2P1P2					
2.0	17585	514.83	450.74	925.47	34.29
1.5	30851	515.37	451.07	925.71	34.36
1.0	68633	516.08	451.31	926.34	34.45
0.75	121366	516.24	451.31	926.30	34.50
0.5	270348	516.47	451.40	926.30	34.54
Sepran PF P2P2					
2.0	17585	515.07	450.92	926.03	34.28
1.5	30851	515.54	451.20	926.11	34.35
1.0	68633	516.17	451.37	926.56	34.45
0.75	121366	516.29	451.34	926.44	34.50
0.5	270348	516.48	451.40	926.37	34.54

Table 5 As Table 4 but now for case 2 with stress- and temperature-dependent viscosity. In this case $z_{\text{io}}=154$.

f_m	T_{ndof}	$T_{(200,-100)}^*$ (°C)	\bar{T}_s^* (°C)	\bar{T}_w^* (°C)	$V_{\text{rms},w}^*$ (mm/yr)
TerraFERMA TH P2P1P2					
2.0	21403	683.05	571.58	936.65	40.89
1.0	83935	682.87	572.23	936.11	40.78
0.5	332307	682.80	572.05	937.37	40.77
Sepran TH P2P1P2					
2.0	17581	681.28	570.26	935.47	41.05
1.5	30947	682.48	570.73	937.11	40.91
1.0	68713	683.07	571.23	940.47	40.92
0.75	121574	682.97	571.62	941.23	41.00
0.5	270668	682.92	572.04	941.28	41.06
Sepran PF P2P2					
2.0	17585	682.38	567.96	936.52	40.67
1.5	30851	683.67	569.60	942.73	40.63
1.0	68633	683.61	571.86	941.18	40.87
0.75	121366	683.03	571.77	940.32	40.98
0.5	270348	682.38	571.44	939.73	41.06

1208

1209 2.3.7 Comparison of the time-dependent solution to that assuming steady state

1210 Solving for the time-dependent solution given the same geometry, boundary con-
 1211 ditions and parameters demonstrates how similar the steady-state and time-
 1212 dependent solutions are after sufficient time in this optimized benchmark. The
 1213 time-dependent slab top temperature evolution until $t^*=A_s^*=25$ Myr is shown in
 1214 Figure 10a and that at the Moho is in Figure 10b. In both cases we plot the tem-
 1215 perature to the depth that the subducting slab will have reached after a given time

1216 interval. The temperature curves show a gradual convergence to the steady-state
1217 solution (the dashed line). The temperature at 25 Myr is given in Figure 10c (com-
1218 pare with Figure 9d) and the temperature difference between that at 25 Myr and
1219 the steady-state case is shown in Figure 10d – clearly the forearc thermal structure
1220 is the slowest part of the model to adjust to steady state.

1221 The benchmark has been designed to give a near-steady-state solution close to
1222 the time-dependent solution after 25 Myr. However this similarity is not generally
1223 the case in other geometries so time-dependent solutions remain necessary when
1224 considering a larger suite of models and therefore form the bulk of the results
1225 presented in part III. Due to the slow evolution of the subduction system we found
1226 in the time-dependent version of the benchmark that fully converging the residual,
1227 \mathbf{r} , was not necessary for an accurate solution, making extremely minor differences
1228 after 25 Myr of evolution. Linearizing the problem and only taking a single Picard
1229 iteration at each time level represents a considerable computational cost saving
1230 so we adopt that approach in part III. TerraFERMA results are presented using
1231 $\theta_v = \theta = 0.5$. Sepran uses $\theta_v = \theta = 1$ and both use $c_{\text{crit}} = 1$ in all time-dependent results
1232 shown there.

1233 3 Conclusions

1234 By constructing a series of demonstration problems we have shown how finite ele-
1235 ment models can be constructed, tested, and validated. Once validated these simpler
1236 systems of equations can be used as building blocks to develop a kinematic-dynamic
1237 model of subduction zone thermal structure. We propose a new benchmark problem
1238 for subduction zones that incorporates more of the physical complexity associated
1239 with their thermal structure while avoiding some of the pitfalls associated with
1240 nonphysical geometries and assumptions of the original van Keken et al. (2008)
1241 benchmark. This has been demonstrated with two independent finite element ap-
1242 proaches (TerraFERMA and Sepran) that also use different discretization strate-
1243 gies. In part III we will use these models and apply the discretization and solution
1244 strategies described here to a global suite of subduction zones. We will discuss where
1245 they agree and disagree, both with each other and with published observations of
1246 subduction zone thermal structure.

1247 Abbreviations

1248 DOFs: Degrees of Freedom; FEM: Finite element method; SZ: subduction zone; TF: TerraFERMA; UFL: Unified
1249 Form Language

1250 Availability of data and material

1251 The modeling data shown in the figures are provided in the zenodo repository available at
1252 doi.org/10.5281/zenodo.7843967. The TF modeling data can be independently reproduced using the input files
1253 provided in https://github.com/cianwilson/vankeken_wilson_peps_2023, which can be run using the docker images
1254 contained in https://github.com/users/cianwilson/packages/container/package/vankeken_wilson_peps_2023. The
1255 zenodo repository contains all files and information listed as Supplemental Information.

1256 Competing interests

1257 The authors declare that they have no competing interest.

1258 Funding

1259 This work was supported in part by National Science Foundation grants 1850634 and 2021027 to PvK.

1260 Authors' contributions

1261 Both authors conceived of the approach to the review paper. CW provided the main modeling using TF, PvK
1262 provided the Sepran-based models. Both authors contributed to writing this paper.

1263 **Acknowledgements**

1264 We thank editor Magali Billen and two anonymous reviewers for many helpful and constructive comments &
 1265 questions that allowed us to improve the manuscript. We thank Scott King for comments on an earlier version of
 1266 the manuscript.

1267 **References**

- 1268 Alnæs, M.S, Logg, A, Ölggaard, K.B, Rognes, M.E, Wells, G.N (2014) Unified form language: A domain-specific
 1269 language for weak formulations of partial differential equations. *ACM Trans Math Softw* 40, 1–37.
 1270 doi:10.1145/2566630
- 1271 Alnæs, M.S, Blechta, J, Hake, J, Johansson, A, Kehlet, B, Logg, A, Richardson, C, Ring, J, Rognes, M.E, Wells,
 1272 G.N (2015) The FEniCS project version 1.5. *Arch Num Soft* 3, 9–23. doi:10.11588/ans.2015.100.20553
- 1273 Auricchio, F, Beirão da Veiga, L, Brezzi, F, Lovadina, C (2017) Mixed finite element methods. In: Stein, E, Borst,
 1274 R, Hughes, T.J.R (eds.) *Encyclopedia of Computational Mechanics Second Edition*. John Wiley & Sons,
 1275 Ltd, Chichester, UK, pp 1–53. doi:10.1002/9781119176817.ecm2004
- 1276 Balay, S, Abhyankar, S, Adams, M.F, Benson, S, Brown, J, Brune, P, Buschelman, K, Constantinescu, E.M,
 1277 Dalcin, L, Dener, A, Eijkhout, V, Faibusowitsch, J, Gropp, W.D, Hapla, V, Isaac, T, Jolivet, P, Karpeev,
 1278 D, Kaushik, D, Knepley, M.G, Kong, F, Kruger, S, May, D.A, McInnes, L.C, Mills, R.T, Mitchell, L,
 1279 Munson, T, Roman, J.E, Rupp, K, Sanan, P, Sarich, J, Smith, B.F, Zampini, S, Zhang, H, Zhang, H,
 1280 Zhang, J (2023) PETSc Web page. <https://petsc.org/>
- 1281 Batchelor, G.K (1967) *An Introduction to Fluid Dynamics*. Cambridge University Press, Cambridge, UK
- 1282 Blankenbach, B, Busse, F, Christensen, U, Cserepes, L, Gunkel, D, Hansen, U, Harder, H, Jarvis, G, Koch, M,
 1283 Marquart, G, Moore, D, Olson, P, Schmeling, H, Schnaubelt, T (1989) A benchmark for mantle convection
 1284 codes. *Geophys J Int* 98, 23–38. doi:10.1111/j.1365-246X.1989.tb05511.x
- 1285 Burstedde, C, Stadler, G, Alisic, L, Wilcox, L.C, Tan, E, Gurnis, M, Ghattas, O (2013) Large-scale adaptive
 1286 mantle convection simulation. *Geophys J Int* 192, 889–906. doi:10.1093/gji/ggs070
- 1287 Cuvelier, C, Segal, A, van Steenhoven, A.A (1986) *Finite Element Models and the Navier-Stokes Equations*.
 1288 Reidel, Dordrecht, The Netherlands
- 1289 Dabrowski, M, Krotkiewski, M, Schmid, D.W (2008) MILAMIN: MATLAB-based finite element method solver for
 1290 large problems. *Geochem Geophys Geosys* 9. Art No Q04030, doi:10.1029/2007GC001719
- 1291 Davies, D.R, Wilson, C.R, Kramer, S.C (2011) Fluidity: A fully unstructured anisotropic adaptive mesh
 1292 computational modeling framework for geodynamics. *Geochem Geophys Geosys* 12. Art No Q06001,
 1293 doi:10.1029/2011GC003551
- 1294 Davies, R.D, Kramer, S.C, Ghelichkhan, S, Gibson, A (2022) Towards automatic finite-element methods for
 1295 geodynamics via Firedrake. *Geosci Model Devel* 15, 5127–5166. doi:10.5194/gmd-15-5127-2022
- 1296 Euen, G.T, Liu, S, Gassmöller, R, Heister, T, King, S.D (2022) A comparison of 3-D spherical shell thermal
 1297 convection results at low to moderate Rayleigh number using ASPECT (version 2.2.0) and CitComS
 1298 (version 3.3.1). *Geosci Model Devel Disc*. doi:10.5194/gmd-2022-252
- 1299 Fullsack, P (1995) An arbitrary Lagrangian-Eulerian formulation for creeping flows and its application in tectonic
 1300 models. *Geophys J Int* 120, 1–23. doi:10.1111/j.1365-246X.1995.tb05908.x
- 1301 Gerya, T (2019) *Introduction to Numerical Geodynamical Modelling, Second Edition*. Cambridge University Press,
 1302 Cambridge, UK
- 1303 Golub, G.H, Van Loan, C.F (1989) *Matrix Computations, 2nd Edition*. Johns Hopkins University Press, Baltimore,
 1304 MD, USA
- 1305 Hall, P.S (2012) On the thermal evolution of the mantle wedge at subduction zones. *Phys Earth Planet Int*
 1306 198–199, 9–27. doi:10.0116/j.pepi.2012.03.004
- 1307 Ham, D.A, Farrell, P.E, Gorman, G.J, Maddison, J.R, Wilson, C.R, Kramer, S.C, Shipton, J, Collins, G.S, Cotter,
 1308 C.J, Piggott, M.D (2009) Spud 1.0: Generalizing and automating the user interfaces of scientific computer
 1309 models. *Geosci Model Dev* 2, 33–42. doi:10.5194/gmd-2-33-2009
- 1310 Ho-Liu, P, Hager, B.H, Raefsky, A (1987) An improved method of Nusselt number calculation. *Geophys J Int* 88,
 1311 205–215. doi:10.1111/j.1365-246X.1987.tb01375.x
- 1312 Hughes, T.J.R (1987) *The Finite Element Method*. Prentice-Hall, Inc., Englewood Cliffs, NJ, USA
- 1313 Ismail-Zadeh, A, Tackley, P (2010) *Computational Methods for Geodynamics*. Cambridge University Press,
 1314 Cambridge, UK
- 1315 Johnson, C (1987) *Numerical Solution of Partial Differential Equations by the Finite Element Method*. Cambridge
 1316 University Press, Cambridge, UK
- 1317 Karato, S-I, Wu, P (1993) Rheology of the upper mantle: A synthesis. *Science* 260, 771–778.
 1318 doi:10.1126/science.260.5109.771
- 1319 King, S.D, Raefsky, A, Hager, B.H (1990) Conman: vectorizing a finite element code for incompressible
 1320 two-dimensional convection in the Earth's mantle. *Phys Earth Planet Inter* 59, 195–207.
 1321 doi:10.1016/0031-9201(90)90225-M
- 1322 King, S.D, Lee, C, van Keken, P.E, Leng, W, Zhong, S, Tan, E, Tosi, N, Kameyama, M.C (2010) A community
 1323 benchmark for 2-D Cartesian compressible convection in the Earth's mantle. *Geophys J Int* 180, 73–87.
 1324 doi:10.1111/j.1365-246X.2009.04413.x
- 1325 Kirby, R.C, Logg, A (2006) A compiler for variational forms. *ACM Trans Math Softw* 32, 417–444.
 1326 doi:10.1145/1163641.1163644
- 1327 Kronbichler, M, Heister, T, Bangerth, W (2013) High accuracy mantle convection simulation through modern
 1328 numerical methods. *Geophys J Int* 191, 12–29. doi:10.1111/j.1365-246X.2012.05609.x
- 1329 Logan, D.L (2017) *A First Course in the Finite Element Method, Sixth Edition*. Cengage, Boston, MA, USA
- 1330 Logg, A, Mardal, K-A, Wells, G (2012) *Automated Solution of Differential Equations by the Finite Element
 1331 Method*. Springer, Berlin, Germany
- 1332 Moresi, L, Quenette, S, Lemiale, V, Mériaux, C, Appelbe, B, Mühlhaus, H-B (2007) Computational approaches to
 1333 studying non-linear dynamics of the crust and mantle. *Phys Earth Planet Inter* 163, 69–82.

- 1334 doi:10.1016/j.pepi.2007.06.009
- 1335 Oden, J.T, Reddy, J.N (1976) *An Introduction to the Mathematical Theory of Finite Elements*. John Wiley and
- 1336 Sons, New York, NY, USA
- 1337 Strang, G, Fix, G (2008) *An Analysis of the Finite Element Models*, 2nd Edition. Wellesley Cambridge Press,
- 1338 Wellesley, MA, USA
- 1339 Syracuse, E.M, van Keken, P.E, Abers, G.A (2010) The global range of subduction zone thermal models. *Phys*
- 1340 *Earth Planet Int* 183, 73–90. doi:10.1016/j.pepi.2010.02.004
- 1341 Turcotte, D, Schubert, G (2002) *Geodynamics*, 2nd Edition. Cambridge University Press, Cambridge, UK
- 1342 van den Berg, A.P, Segal, G, Yuen, D.A (2015) SEPRAN: A versatile finite-element package for a wide variety of
- 1343 problems in geosciences. *J Earth Sci* 26, 89–95. doi:10.1007/s12583-015-0508-0
- 1344 van Keken, P.E, Wilson, C.R (2023) An introductory review of the thermal structure of subduction zones: I –
- 1345 motivation and selected examples. *Prog Earth Planet Sci* 10. Art No 42, doi:10.1186/s40645-023-00573-z
- 1346 van Keken, P.E, Kiefer, B, Peacock, S.M (2002) High-resolution models of subduction zones: Implications for
- 1347 mineral dehydration reactions and the transport of water to the deep mantle. *Geochem Geophys Geosys* 3.
- 1348 Art No 1056, doi:10.1029/2001GC000256
- 1349 van Keken, P.E, Currie, C, King, S.D, Behn, M.D, Cagnioncle, A, He, J, Katz, R.F, Lin, S-C, Parmentier, E.M,
- 1350 Spiegelman, M, Wang, K (2008) A community benchmark for subduction zone modeling. *Phys Earth Planet*
- 1351 *Int* 171, 187–197. doi:10.1016/j.pepi.2008.04.015
- 1352 van Keken, P.E, Hacker, B.R, Syracuse, E.M, Abers, G.A (2011) Subduction factory: 4. Depth-dependent flux of
- 1353 H₂O from subducting slabs worldwide. *J Geophys Res: Solid Earth* 116. Art No B01401,
- 1354 doi:10.1029/2010JB007922
- 1355 Vynnytska, L, Rognes, M.E, Clark, S.R (2013) Benchmarking FEniCS for mantle convection simulations. *Comp*
- 1356 *Geosci* 50, 95–105. doi:10.1016/j.cageo.2012.05.012
- 1357 Wada, I, Wang, K (2009) Common depth of slab-mantle decoupling: Reconciling diversity and uniformity of
- 1358 subduction zones. *Geochem Geophys Geosys* 10. Art No Q10009, doi:10.1029/2009GC002570
- 1359 Wilson, C.R, Spiegelman, M.S, van Keken, P.E (2017) TerraFERMA: The Transparent Finite Element Rapid
- 1360 Model Assembler for multiphysics problems in Earth sciences. *Geochem Geophys Geosys* 18, 769–810.
- 1361 doi:10.1002/2016GC006702
- 1362 Zhong, S.J, Yuen, D.A, Moresi, L.N, Knepley, M.G (2015) Numerical methods for mantle convection. In:
- 1363 Schubert, G (ed.) *Treatise on Geophysics* (2nd Edition), Volume 7 "Mantle Dynamics" (Bercovici, D (ed.))
- 1364 pp 197–222. Elsevier, Amsterdam, The Netherlands. doi:10.1016/B978-0-444-53802-4.00130-5
- 1365 Zhong, S, McNamara, A, Tan, E, Moresi, L, Gurnis, M (2008) A benchmark study on mantle convection in a 3-D
- 1366 spherical shell using CitcomS. *Geochem Geophys Geosys* 9. Art No Q10017, doi:10.1029/2008GC002048

Figure 10 Time-dependent example based on the new subduction zone benchmark. a) Evolution of slab top temperature as a function of time – curves are plotted only to the depth that the slab tip has reached at each time; b) As a) but now for the slab Moho; c) Temperature at 25 Myr (compare to steady-state thermal structure in Figure 9d); d) Difference between temperature of the time-dependent solution after 25 Myr and the steady-state solution – while the slab thermal structure is nearly identical, the cold corner is still evolving at 25 Myr towards the steady-state structure. Star indicates the location of the coupling point or its steady-state temperature.

